

# Electrodeposition-enabled, electricallytransduced sensors and biosensors

Eric J. Choi<sup>1</sup>, Nicholas P. Drago<sup>1</sup>, Nicholas J. Humphrey<sup>1</sup>, Justin Van Houten<sup>2</sup>, Jaewan Ahn<sup>3</sup>, Jiyoung Lee<sup>3</sup>, Il-Doo Kim<sup>3</sup>, Alana F. Ogata<sup>2</sup>, Reginald M. Penner<sup>1</sup>,

Electrodeposition and electropolymerization have emerged as versatile tools for the fabrication of chemical and biosensors. The literature in this area, published since 2017, is the main focus of this review. Electropolymerization has played a particularly prominent role in sensor development since its discovery in 1980 by Diaz at IBM. The ability to entrain receptors such as antibodies, engineered virus particles, and metal chelating agents into a conductive polymer sensing element during electropolymerization has proven to be a powerful means of preparing chemiresistors for a variety of analyses. Electrodeposition has also been used to prepare nanostructured metal indicator microelectrodes, enabling of a new modality for transducing biosensors. Electrodeposited metal nanowires have formed the basis for rapid and sensitive sensors for hydrogen gas. Electrodeposition has also been exploited as a powerful means for amplifying weak biosensor signals, extending their dynamic range. Opportunities for the application of electrodeposition and electropolymerization for chemical and biological sensor fabrication and function are discussed.

Keywords: Electrochemistry; Electropolymerization; Transduction; Wearable; Nanowire; Nanoparticle; Gas sensor; Amplification

## Introduction

Electrodeposition (ED) is now more than two centuries old, but its application to the fabrication and function of sensors and biosensors is relatively recent. Only since 1980 has ED, and its relative, electropolymerization (EP), been exploited to enhance the properties of sensors and biosensors. In these applications, the three attributes of ED are: i) Precision, ii) Selectivity, and iii) Compatibility. ED allows precise control of the quantity of electrodeposited material, of composition, of particle size, of surface roughness, and in some cases, control of the porosity of the electrodeposit. ED and EP also afford the ability to prepare

composites containing two or more materials such as an antibody, a chelator, a single-stranded DNA (ss-DNA), or other receptors.

The *precision* intrinsic to ED is, itself, an attribute: The fine control afforded in ED using current and potential is difficult to match using alternative deposition methods, such as physical vapor deposition, sputtering, spin-coating, spraying, imprinting, and so on. A second attribute is that ED imparts spatial *selectivity* to the ED process because the deposition process can be targeted at, and confined to, a single conductor amongst other sensor components. For example, a polymer film can be EDed onto a metal transducer without risking contamination of other sensor parts with this material. Moreover, ED and EP can be carried out on conductors that are immersed in aqueous plating solutions. This means that biological materials such as proteins, antibodies,

E-mail addresses: Kim, I.-D. (idkim@kaist.ac.kr), Ogata, A.F. (alana.ogata@utoronto.ca), Penner, R.M. (rmpenner@uci.edu).

1369-7021/© 2022 The Authors. Published by Elsevier Ltd. https://doi.org/10.1016/j.mattod.2022.11.021This is an open access article under the CC BY license (http://creativecommons.org/licenses/by/4.0/).

<sup>&</sup>lt;sup>1</sup> Department of Chemistry, University of California, Irvine, CA 92697-2025, United States

<sup>&</sup>lt;sup>2</sup> Department of Chemical and Physical Sciences, University of Toronto, Mississauga, ON L5L 1C6, United States

<sup>&</sup>lt;sup>3</sup> Department of Materials Science and Engineering, Korea Advanced Institute of Science and Technology (KAIST), 291 Daehak-ro, Yuseong-gu, Daejeon 34141, Republic of Korea

<sup>\*</sup> Corresponding authors.

and aptamers can be co-deposited using ED and EP. This *compatibility* of ED and EP with aqueous solutions, has been a major driver of the application of ED and EP to the fabrication and function of biosensors.

The combination of precision, selectivity, and compatibility have made ED and EP advantageous in many processes, leading to the growth in the application of these methods. As an indicator of the research activity in this area, a Google Scholar search on "sensor and electrodeposition" returns 115,000 publications (August 3, 2022). The majority of the literature highlighted and discussed in this review are publications since 2017. We further confine the scope of this review to *electrically transduced* sensors in alignment with the expertise of our own research groups. Even with these constraints, this growing literature is already too expansive for an exhaustive review. The goal of this review is to illuminate the most important and impactful trends.

## A brief history

A pictorial timeline (Fig. 1) lists some milestones marking progress related to the application of ED to sensor and biosensor development prior to 2017.

## Electronically conductive polymers

This chronology begins with chemiresistive sensors in which electronically conductive organic polymers functioned as either receptors or transducers or both. In 1980, Art Diaz and coworkers at IBM discovered that heterocycles including pyrrole, thiophene, and aniline could be electropolymerized to form conductive films simply by oxidizing solutions containing these monomers [1–5]. This process, known as electropolymerization (EP), helped the initial development of ED-enabled sensors. Diaz and coworkers demonstrated that electrodeposited films of poly (pyrrole) (PPY), poly(thiophene), and poly(aniline) (PANI)

showed electrochromic behaviors and strongly modulated electronic conductivity that were both correlated with the redox electrochemistry of these films.

By 1986, these electropolymerized polymers, such as (poly(3-methyl-thiophene) [6], and their derivatives, including poly(3,4 ethylene dioxythiophene) (PEDOT) [7], were exploited for the fabrication of sensors and biosensors targeting a range of molecules. Art Janata, a pioneer in the development of a field-effect transistor (FET) based chemical sensors [8–10], reported a solid-state alcohol vapor sensor based upon a suspended-gate FET (SGFET) in which a platinum (Pt) gate modified by electrode-posited PPY, as well as several derivatives, sensitized the SGFET to a series of primary alcohols with response times within seconds [11]. Likewise, PPY was being widely applied to gas sensors [12] and biosensors [13,14] in the same time period.

Foulds and Lowe [15] were among the first to incorporate enzymes into PPY by co-electrodeposition/electropolymeriza tion. This strategy was applied in 1986 to prepare an amperometric glucose sensor based upon the incorporation of glucose oxidase into PPY [15].

#### Metal and polymer nanowires

The next class of transducers/receptors to emerge were onedimensional nanowires based on metals and polymers, by virtue of their high specific surface area that promotes a more sensitive detection of analytes compared to the film-type sensors. This was kickstarted in 2001 by the development of a nanowire ED method termed electrochemical step edge decoration (ESED) [16,17], which involved the nucleation and growth of the electrodeposited metal on the step edges of highly oriented graphite electrodes. These nanowire networks were then transferred from the graphite surface onto a glass slide by embedding them in a polymer film. Silver (Ag) epoxy was then used to establish electri-

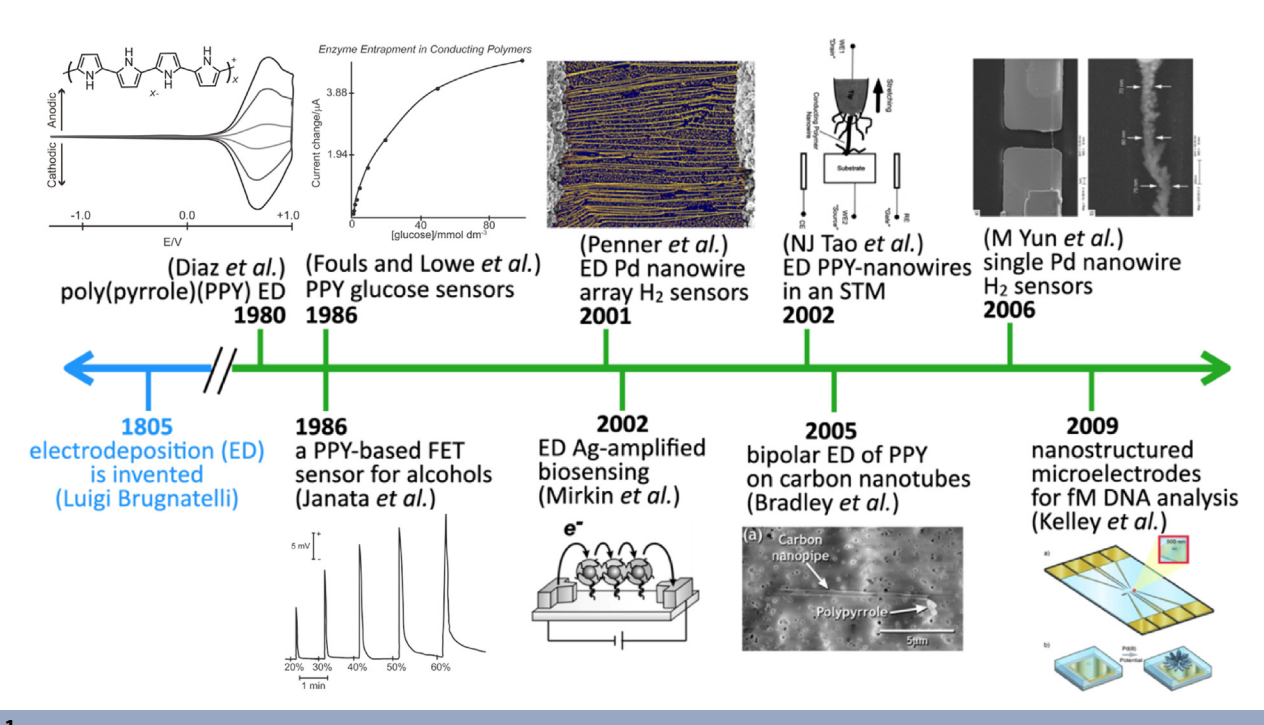


## FIGURE 1

Milestones in ED and EP-enabled electrically-transduced chemical sensing and biosensing. The references highlighted here can be found in Section "Introduction".

cal contacts to these nanowire networks. Palladium (Pd) nanowire networks prepared by ESED comprised the first palladium nanowire hydrogen gas sensors [18,19].

In parallel with this discovery, the first-ever successful synthesis of polymer nanowires prepared by a modified EP process was described by Nongjian Tao and colleagues in 2002 [20]. Their approach involved the application of a tip in a scanning tunneling microscope. The surface of the conductive substrate and the tip were both poised at a potential exceeding that of the onset for PANI polymerization from aniline. As this polymerization proceeded at both the tip and surface, the gap between these elements was bridged, forming a nanowire [20].

In 2004, Yun, Myung, and others demonstrated the preparation of single PPY and Pd nanowires by EP and ED, respectively [21,22]. In 2006, single Pd nanowire chemiresistors prepared using this method were used for the detection of H<sub>2</sub> gas for the first time [23]. Bradley and coworkers [24] demonstrated that carbon nanotubes could be decorated with PPY without making a direct electrical connection to the nanotube using a bipolar electrodeposition method. PPY decoration of carbon nanotubes provided a means for controlling how much water these structures could be filled with [24].

## Signal transduction and amplification

An innovation in 2002 was the discovery by Mirkin *et al.* [25] that immunogold staining methods that have been developed for microscopy [26], in which Ag is grown on gold (Au) labels by electroless deposition to increase contrast, could be used to provide amplification of sandwich assays involving a Au nanoparticle label. In these experiments, a ss-DNA capture strand was recognized by a complimentary ss-DNA probe strand conjugated to a Au nanoparticle, at concentrations as low as 0.5 pM. In this experiment, ss-DNA capture strands are located between two lithographically patterned Au electrodes that measure a percolating current across this affinity layer as Ag deposition onto the immobilized Au nanoparticles increased the measured current between these electrodes [25].

Subsequently, in 2009, Su *et al.* [27] exploited the same scheme for the detection, using a quartz crystal microbalance (QCM) as the transducer. In this work, the detection sensitivity of human IgG (h-IgG) was enhanced by 100 times in a sandwich assay involving an Au nanoparticle-labeled anti-h-IgG after applying solution-phase electroless Ag plating process for 20 min [27].

#### Lithographically patterned nanowire electrodeposition

A significant technological advance was made in 2006 through the development of the lithographically patterned nanowire electrodeposition (LPNE) process, which can be used to prepare high-quality metal nanowire arrays [28,29]. In contrast to the ESED process that was reported in 2001 [16,17], LPNE allowed the position of a nanowire to be precisely determined using a photolithographic process. Importantly, the nanowire dimensions were controlled by processing steps that were not affected by the diffraction of light, enabling the fabrication of subwavelength, nanometer-scale wires [28,29]. Compared with the process of Yun and Myung (2006) that only allowed the synthesis of single strands of polymer and metal nanowires one at a

time [21,22], LPNE provided for the deposition of any number of nanowires in parallel, in virtually any pattern achievable by photolithography [28,29]. LPNE was first used to prepare  $H_2$  sensors based on single Pd nanowires in 2009 with improved performance compared to previously reported Pd-based sensors [30].

#### Nanostructured metal microelectrodes

The development in 2009 [31–33] of ED-prepared nanostructured microelectrode transducers by Shana Kelley became the springboard for a completely new strategy for biosensing [34,35]. In these experiments, highly dispersed metal transducers with micron-scale dimensions were functionalized with ss-DNA and other receptors, and their electrochemical responses to target redox species in solution were monitored. By this, the binding of target species with the immobilized receptors could effectively be transduced into electrical signals. Uniquely, the sensitivity of the nanostructured transducer could be tuned based on its level of dispersion, which was controlled by the electrodeposition parameters used for its preparation [33].

## Fundamental advances in electropolymerization

As demonstrated in the timeline of Fig. 1, EP has played a particularly prominent role in the development of ED-enabled sensor science and technology. Innovations in ED that specifically impact the sensing characteristics will be the focus of discussion throughout this review (Sections "Sensors for Solution-phase Analvsis, Gas Sensors, Wearable sensors, and ED-based Signal Transduction/Amplification"). Particularly in Section "Fundamental Advances in Electropolymerization", we introduce the fundamental chemistry and mechanisms of EP (Section "EP mechanisms"), followed by bipolar EP processes (Section "An innovation in EP: Bipolar EP"), to provide a general understanding of the impactful advancements made regarding the EP technology. We return to discussing EP in later Sections "Polymeric sensing elements, Electronically conductive polymers, and Wearable sensors," to discuss the application of EP in recent sensing applications and architectures.

#### **EP Mechanisms**

Most work involving electrodeposited polymers utilizes the *in situ* polymerization step as a method to synthesize hybrid materials, such as metal-complex polymers [36–42], nanomaterial-polymer [43–47], and biological-polymer composites [48–53] with potential for enhanced sensing platforms. Recent advances in EP have been achieved through the advent of advanced analytical techniques to elucidate EP mechanisms. Additionally, as will be discussed in the next section, the application of bipolar electrochemistry for EP has produced a new field of bipolar EP for the synthesis of linear or highly branched polymer wires and films.

The development of advanced microscopy techniques has enabled high-resolution studies of the EP process and revealed mechanisms of polymer growth. Sakaguchi *et al.* [54] investigated the electropolymerization of thiophene monomers, 3-octyloxy-4-methylthiophene (C8OMT) and 3-octyl-4-methylthiophene (C8MT), using scanning tunneling microscopy (STM) which enables imaging of the organics at single-molecule resolutions [54]. Electropolymerization of C8OMT *via* applica-

tion of voltage pulses produced arrays of uniform nanowires up to 100 nm in length, while the same for C8MT resulted in single nanowires with a dotted pattern having 11.5-angstrom spacings in between the nodes. Structural differences were attributed to the influence of the electronic structures of each thiophene monomer. Specifically, C8MT showed a larger HOMO (Highest Occupied Molecular Orbital)-LUMO (Lowest Unoccupied Molecular Orbital) gap, which can be ascribed to the torsion of the thiophene ring. Utilizing this discovery, the authors demonstrated a two-step electropolymerization process starting with the polymerization of C8MT and followed by the simultaneous polymerization of C8MT and C8OMT, which enabled a block polymerization process that produced multiblock polymer nanowires. Following the creation of heterojunctions between the C8MT-polymer and C8OMT-polymer wires, sequential STM was applied to study the chemical bonding and polymer diffusion at the heterojunctions [54].

In 2021, Subramanian et al. [55] studied the EP of polyethylene-dioxythiophene (PEDOT) using in situ liquid phase transmission electron microscopy (LPTEM) to probe the relationships between the choice of counter ion in the electrolyte solution and the final PEDOT morphology [55]. During the EP of PEDOT, the presence of poly(acrylic acid) (PAA) counter ions induce the formation of PEDOT nanofibrils with a thick nanofibril core and a thin outer edge. Authors observed that the growth kinetics of nanofibrils, which were ultimately 1-2 μm in length and 200-250 nm thick, occurred in three stages spanning a total period of about 180 s: (1) formation of nucleation sites and local precipitation (2) fast anisotropic growth of nucleated sites into long fibrils growing perpendicular to the electrode surface, and (3) decreased growth rate in lengthwise and expedited growth in fibril thickness. The authors hypothesize that the coating of PEDOT with PAA, which is electrically insulating, locally impedes the EP process and prevents lateral growth. In general, such additives can be an effective experimental parameter to control nanofibril morphology.

Additionally, while pyrrole is a widely studied electropolymerized monomer, several new mechanisms have recently been proposed for the EP of pyrroles. Herlem *et al.* [56] presented molecular dynamic simulations to examine the preliminary steps in the EP of three pyrrole molecules on a charged Pt surface in an aqueous electrolyte, using an effective screening method [56]. Simulations based on the laws established by a density-functional theory framework elucidated the formation of a cation-radical on pyrrole and its subsequent reaction with neighboring pyrrole molecules in three different chemical environments (pure DI water, aqueous solution containing  $\mathrm{Cl}^-$ , and aqueous solution containing  $\mathrm{BF}_4^-$ ). Simulations support that only non-nucleophilic salts enable the complete migration of the polarons for chain migration in the pyrrole molecules during EP.

#### An innovation in EP: Bipolar EP

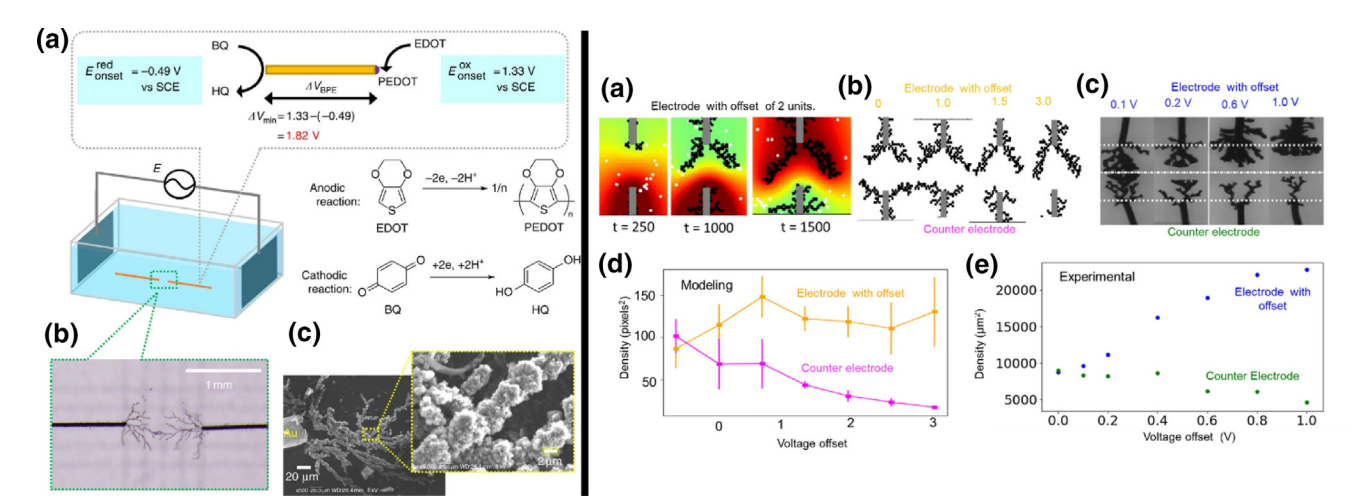
Bipolar ED and EP are processes that induce Faradaic electrochemistry at a bipolar electrode that is immersed in electrolyte containing redox species, but in a wireless manner without any direct connections to a voltage source. Bipolar electrochemistry (BPE) occurs when a voltage applied between two other electrodes in the same solution, called driving electrodes – located

on opposite sides of the bipolar electrode - creates an electric field that produces a voltage drop (iR) across the length of the conductor, that which is large enough to drive simultaneous anodic and cathodic reactions at its positively and negatively polarized edges [57].

BPE was first discussed in the 1960s when Fleischmann, Goodridge, Wright, and coworkers described the application of a voltage between two driving electrodes to produce fluidized bed electrodes [58,59]. However, over the past few decades, there has been a renewed interest in BPEs for application in EP, beginning with the 2005 work of Bradley *et al.* [24] regarding the EP of polypyrrole on the tip of carbon nanotubes [24]. For comprehensive reviews on bipolar electrochemistry and their impacts on chemical analysis, the reader is referred to the following reviews as cited [60–64].

In alternating current (AC) bipolar EP, an AC voltage, instead of direct-current, is applied between the driving electrodes, which drives simultaneous anodic polymerization at both ends of the electrode material. AC bipolar EP allows for a unique alternative to synthesizing nanostructured polymer networks observed in soft-template or templateless electropolymerization [65,66]. In 2016, Koizumi et al. demonstrated the first ACbipolar EP of EDOT in between two Au nanowires [67]. Instead of the formation of a thin film as expected from typical EP processes, fibers of PEDOT were synthesized with branched nanostructures and various other morphologies that could be controlled by the EDOT monomer structure as well as the distance between two Au wires (Fig. 2, left). In a subsequent study, the authors studied the effect of electrolytic conditions, such as monomer concentration, applied frequency, monomer structure, and substrate material, on the AC-bipolar EP of PEDOT [68]. Under optimized conditions, PEDOT structures propagated out from the Au wire into branched dendritic structures. Also, the frequency of the applied AC potential could be varied to tailor the structure even further: thin films were observed at low frequency (1 Hz) while thin branched dendritic structures were observed at high frequencies (15 and 50 Hz). The authors proposed that high EDOT concentrations at the electrode surface produce a large amount of PEDOT that extends onto the glass substrate to form a thin film. Low frequencies would enable large PEDOT growth at each pulse, also resulting in thin films.

In a 2020 study, Shida et al. [69] showed that PEDOT films obtained by AC-bipolar EP exhibited anisotropic behaviors. PEDOT branched structures were studied in the presence of Pt and Al electrodes, which exhibited Ohmic and Schottky properties, respectively. By varying the position along the electrodes, the existence of a position-dependent ionization potential was revealed, which was attributed to a gradient in the doping concentration as a result of bipolar EP. Therefore, within one bipolar electropolymerized PEDOT film, a gradient of electrochemical states was present from neutral to doped throughout the branched structures. In 2021, Janzakova et al. [70] investigated the growth of bipolar electropolymerized PEDOT dendrites with focus on the morphological changes in interconnected nodes observed for these polymers for application in biomimetic dendrite formation. The authors investigated the effect of peak voltage amplitude (Vp), voltage offset, and frequency of voltage pulses. A higher V<sub>p</sub> resulted in larger projected areas, higher frac-



(**left**) (a) Schematic representation of the electrochemical setup for AC-bipolar electrolysis including oxidative polymerization of EDOT and sacrificial reduction of BQ with Au wires ( $\varphi = 50 \mu m$ , 20 mm) as BPEs set in between Pt driving electrodes ( $20 \times 20 \mu m$ , distance: 60 mm), (b) optical microscope image of PEDOT fibers bridging the 1 mm gap between Au wires ( $\Delta V_{BPE} = 8.3 V$ , 90 s) and, (c) SEM images of the PEDOT fibers. HQ, hydroquinone; SCE, saturated calomel electrode. Reproduced with permission from reference [67], copyright 2016 Springer Nature. (**right**) (a) The growth process of dendrites along with spatiotemporal map for voltage offset of 2 voltage units, demonstrating higher attraction of particles towards the electrode with offset. (b) Modeling images of morphologies for voltage offset of 0–3 voltage units. (c) Experimental images of dendrites morphologies at voltage offsets of 0.1–1 V. (d) Dendrite density comparison for the modeling images for the electrode with offset (shown in orange) and counter electrode (shown in magenta). (e) Dendrite density comparison for the experimental images for the electrode with offset (shown in blue) and counter electrode (shown in green). Reproduced with permission from reference [71], copyright 2022 Springer Nature.

tal number, and a maximum of five branches. Introducing a voltage offset produced anodic and cathodic voltage asymmetry between both wires, wherein the wire experiencing lower applied oxidation voltages produced thin, linear, dendrites, while the wire with higher applied oxidation voltages produced thick and branched dendrites. PEDOT electropolymerized at low frequencies resulted in large, thick, branched dendrites, and those prepared with mid-range frequencies produced thin branched dendrites, while those based on higher frequencies produced thin wires. Electropolymerized PEDOT was applied to microelectrode arrays for demonstrating that dendritic PEDOT structures can be used to program an array, self-connecting an output using electrical event-based dendritic interconnectivity. To further elucidate the mechanisms of bipolar EP that result in different morphologies, Kumar et al. [71] provided a model of the spatiotemporal mapping of the electric field in the liquid during EP. The authors investigated the electric-field dependence on frequency, voltage offset, motion of constituent particles, and polymerization at the electrodes. Authors corroborate the observation that low frequencies of the applied AC voltage resulted in dense, highly branched dendrites while higher frequencies resulted in thin and linear wires, and voltage offsets produced asymmetrical morphologies (Fig. 2, right). These growth processes are dictated by the particle's concentration, trajectory, and distribution, with a large contribution from scattering that slowed down the polymer growth.

## Sensors for Solution-phase analysis

Historically, solution-phase sensors have been used for the measurement of many types of analytes including metal ions [72–74], pesticides [75–77], pathogens [78,79], and chemical warfare agents [80]. More recently, as biomarkers are discovered for a

growing number of diseases, diagnostics research has been accelerated to meet the challenge of disease diagnoses and monitoring as well as a tool for optimizing disease treatments for patients [81–83]. All of these applications require measurements in aqueous solutions, such as ground water and extracts of foods or soils, or in diluted or undiluted bodily fluids, such as blood and urine.

Solution-phase sensors based on polymeric sensor elements (Section "Polymeric sensing elements"), and metals, metal oxides, and other inorganic materials (Section "Metals, metal oxides, and other inorganic materials") are discussed in separate subsections. A brief summary of solution-phase sensors enabled by EP and ED are summarized in Tables 1 and 2.

#### Polymeric sensing elements

Sensors with polymeric sensing elements typically incorporate a receptor such as an antibody, an aptamer, a metal chelator, in order to impart selectivity to the recognition and binding process for a particular analyte species. The incorporation of a receptor, also referred to as the recognition element (hereafter, RE), is commonly accomplished by encapsulation in the polymer matrix during EP (Section "Entrapped/encapsulated recognition elements") by physical and/or chemically imprinting the polymer matrix (Section "Imprinted recognition element") or by surface functionalization (Section "Surface immobilized recognition element").

#### Entrapped/encapsulated recognition elements

Wustoni *et al.* [84] encapsulated enzymes including glucose oxidase  $(GO_x)$ , lactate oxidase  $(LO_x)$ , and cholesterol oxidase  $(CO_x)$ , in electropolymerized 3,4-ethylenedioxythiophene (EDOT) and hydroxymethyl EDOT (EDOTOH), to fabricate three different metabolite sensing channels and one reference channel in a single multiplexed organic electrochemical transistors (OECT)

Debugge based selection where some weekled by FI

Analyte	Electrodeposited element	Detection Modality	Limit-of- Detection	Ref.
Glucose	Poly(o-phenylenediamine) (PoPD) with Chronoamperometry current responses of immobilized glucose oxidase (GOx) PoPD-GOx and PPY-LOx films		Glucose: 1 mM	[85]
Lactate	Polypyrrole with immobilized lactate oxidase (LOx)	Open-circuit potential of IrOx layer in solution	Lactate: 1 mM	
рН	Iridium Oxide (IrOx)			
Chlorpyrifos & acetylthiocholine (ATCh)	Polyphenothiazine on ITO, functionalized with CdS	Variations of photoelectrochemical current from electrostatically adsorbed CdS QDs	0.63 μg/mL	[95]
Ascorbic acid	Poly(o-phenylenediamine) MIP with ascorbic acid	OECT channel current response	10 nM	[90]
Glucose Lactate	PEDOT/PEDOTOH/GO <sub>x</sub> PEDOT/PEDOTOH/LO <sub>x</sub>	OECT channel current response	Glucose: 1 μM Lactate & Cholesterol: 100 μM	[84]
Cholesterol	PEDOT/PEDOTOH/CO <sub>x</sub>			
Human influenza A virus (H1N1)	Poly(EDOTOA-co-EDOT) on PEDOT:PSS	OECT channel current response	0.025 HAU	[94]
Dopamine	Polythionine and polypyrrole MIP with dopamine on nanoporous Au	Peak current ratio from oxidation of dopamine and polythionine during DPV	0.1 μΜ	[91]
Escherichia coli O157:H7	Polydopamine MIP with E.coli	Electrochemiluminescence signal of N-GQD labeled <i>E.coli</i>	8 CFU mL <sup>-1</sup>	[166]
Luteolin	Electropolymerized $\beta$ -cyclodextrin ( $\beta$ -CD) MIP with luteolin	Peak currents of DPV curves	0.024 μΜ	[92]
Cefixime (CEF)	Polyaniline MIP with CEF	Peak currents of DPV curves	7.1 nM	[93]
Anti M—13 P8 IgG antibody & Anti-FLAG M2 IgG antibody	PEDOT with entrapped M-13 virus	Changes in film resistance ( $R_{VBR}$ ) extracted from EIS	40 ng/mL & 188 ng/mL	[87]
HSA	PEDOT with entrapped M-13 virus	Changes in film resistance ( $R_{VBR}$ ) extracted from EIS	7.5 nM	[86]
DJ-1	PEDOT with entrapped M-13 virus	Changes in film resistance ( $R_{VBR}$ ) extracted from EIS	10 pM	[48]
E. coli	Electrodeposited magnetic nanoparticle- chitosan film	Changes in the chitosan films redox activity in CVs	Not reported	[167]
Perfluorooctanesulfonate (PFOS)	Poly(o-phenylenediamine) (Po-PD) MIP with PFOS	Peak currents of CV and DPV curves	0.5 nM	[168]

device (Fig. 3a-d). Binding of the target to the enzyme and produces hydrogen peroxide (H<sub>2</sub>O<sub>2</sub>), inducing a measurable increase in the drain current from the functionalized channel electrode as PEDOT channel is oxidized by H<sub>2</sub>O<sub>2</sub> (Fig. 3e). EP facilitates the fabrication of multiple independent micro-channels, each containing a different enzyme that can function without crosstalk (Fig. 3f) [84].

Park et al. [85] provides additional insights into how EP simplifies the fabrication of multi-channel and multiplexed sensors. These authors developed a "Lab-on-a-Needle" technology using lithographically patterned electrodes, onto which the polymeric active materials were electropolymerized and the enzymes were entrapped. Glucose sensing was performed using a Prussian blue/carbon electrode with electropolymerized poly(ophenylenediamine) (PoPD) entrapping glucose oxidase (GO<sub>x</sub>), and lactate sensing was performed with electropolymerized PPY entrapping lactate oxidase (LO<sub>x</sub>). Detection of the analyte in each sensor is via amperometry based upon H<sub>2</sub>O<sub>2</sub> oxidation by Prussian blue. The different polymers were chosen based on PoPD's high diffusivity for small molecules, compared with PPY, for the tuning of the concentration range for each analyte. The LO<sub>x</sub> enzyme saturates at lower concentrations of lactates (<2 mM), so the authors used a low concentration of pyrrole monomer to electropolymerize and entrap the enzyme, creating a densely packed PPY/LO $_x$  layer. This prevented the diffusion of the generated  $H_2O_2$  away from the Prussian blue/carbon electrode and increased the linear range of this sensor to 1–6 mM [85].

Bhasin et al. [48,86,87] demonstrated that label-impedimetric sensing can be performed by entrapping filamentous M−13 virus particles in a PEDOT layer that bridges two Au electrodes (Fig. 4ac). In such "Virus BioResistors (VBRs)", the virus was genetically engineered to display peptides that bind various targets, including human serum albumin (HSA) [86], DJ-1 (a bladder cancer biomarker) [48], and IgG antibodies [87]. During EP, M13 virus are entrapped within the conductive polymer matrix, providing intimate contact between the transducer and the viruses. The authors report that the binding of the target protein onto the peptides displayed on the phage particles increases the electrical impedance of the sensor (Fig. 4d) with high signal-to-noise ratios at low frequency (Fig. 4e). A limit-of-detection of 10 pM was obtained for the sensor based on protein deglycase DJ-1 (DJ-1 or park7), a protein that serves as a bladder cancer biomarker, with response times of < 20 s (Fig. 4f and g). It is proposed that the impedance increase is caused by the breaking of conductive networks of polymer chains (Fig. 4h). Furthermore, this method is fast, label-free, and redox-probe-free. In contrast to OECTs, the VBR is a chemiresistor, a two-terminal device with no reference electrode [48].

TABLE 2

Metal- and metal oxide-based solution-phase sensors enabled by ED.

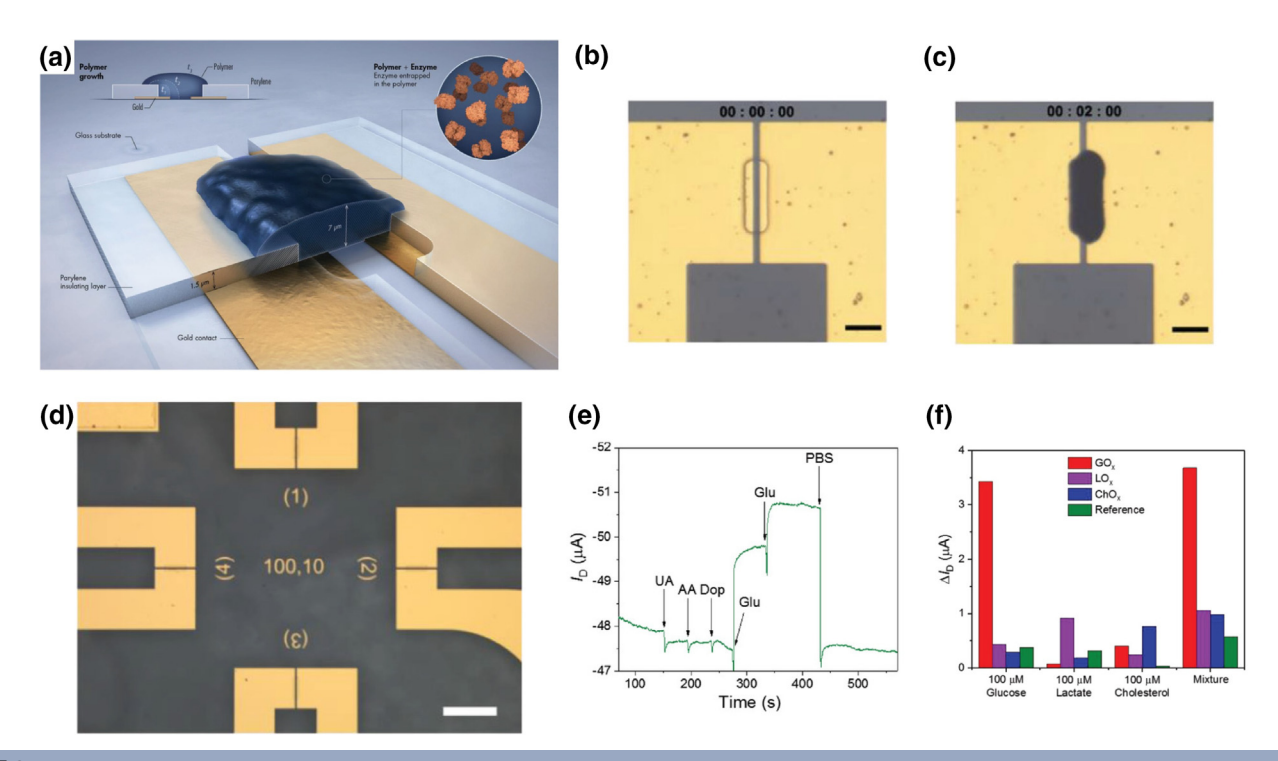
Analyte	Electrodeposited Material	Detection Modality	Limit-of- Detection	Ref
microRNA-21 (miRNA-21)	Hierarchical flower-like Au nanostructures (HFGNs)	Peak currents of Ru(NH <sub>3</sub> ) <sub>6</sub> <sup>3+</sup> from SWV curves	1 fM	[97]
microRNA-21	Au nanoparticles modified with DNA	OECT channel current response	2 pM	[100]
Human heart-type fatty-acid-binding protein (h-FABP)	Ru(bpy) <sub>3</sub> <sup>2+</sup> -functionalized MOF	Electrochemiluminescence signal of encapsulated Ru(bpy) <sub>3</sub> <sup>2+</sup>	150 fg mL <sup>-1</sup>	[113]
Pig IgG	Pt nanoparticles plated on electrochemically assembled Hemin-MOF	Changes in peak currents of DPV curves of the immunoelectrode	0.04 pg mL <sup>-1</sup>	[114]
Surface-protective antigen (Spa) protein			4.3 fg mL <sup>-1</sup>	
Apo-A1	MXene-Ti <sub>3</sub> C <sub>2</sub> T <sub>x</sub> nanosheets	Changes in [Fe(CN) <sub>6</sub> ] <sup>3/4-</sup> redox current in DPV scans	0.3 pg mL <sup>-1</sup>	[115]
NMP 22			$0.7 pg mL^{-1}$	
Glucose	${\rm NiCo_2O_4}$ (NCO) and ${\rm NiCo_2O_4}-{\rm Pd}$ (NCO-Pd) nanosheets	Changes in the oxidation peak current of NCO and NCO-Pd nanosheets	NCO: 2.46 μM NCO-Pd: 0.28 μM	[111]
Human Papilloma Virus 16 (HPV16) DNA	Au nanotube decorated nanoporous polycarbonate (AuNTs-PC)	Charge transfer resistance of [Fe(CN) <sub>6</sub> ] <sup>3/4-</sup> extracted from EIS spectra	1 fM	[105]
Profenofos Phorate Isocarbophos	Aptamer/rGO-CuNPs composite film	Changes in $[Fe(CN)_6]^{3/4-}$ redox current in DPV scans	0.003 nM 0.3 nM 0.03 nM	[169]
Omethoate			0.3 nM	
Epirubicin	Au nanoparticles on Fe <sub>3</sub> O <sub>4</sub> @SiO <sub>2</sub> /DABCO/ SPE	Changes in the material's reduction peak current from LSV scans	0.04 μΜ	[170]
DNA oligonucleotides	Au nanoparticles	OECT channel current response	57.5 fM	[104]
Glucose	Shape-controlled Pd nanoflower-decorated graphene (SPNFG)	FET-type liquid-ion-gated current response	1 nM	[106]
microRNA-21	Au nanoparticles on MoS <sub>2</sub> nanosheets (AuNPs@MoS <sub>2</sub> )	Changes in measured charge via chronocoulometry due to electrostatically bound RuHex	≈100 aM	[101]
Prostate specific antigen	Au nanoparticles on GCE	AuNP-enhanced luminol electrochemiluminescence signal	0.17 pg mL <sup>-1</sup>	[102]
Cancer antigen (CA125)	Hierarchical Au nanostructures	Changes in [Fe(CN) <sub>6</sub> ] <sup>3/4-</sup> redox current in DPV scans	5.5 U mL <sup>-1</sup>	[171]
Malathion	Au nanoparticles on electropolymerized polydopamine on GCE	Changes in ferrocene and thionine electrochemical signals in DPV scans	0.5 ng/L	[103]
Nitrite	Electrodeposited Pd and Pt nanoparticles on porous gallium nitride (Pd-Pt/PGaN)	Amperometric current response of Pd-Pt/PGaN electrode	0.95 μΜ	[107]
рН	IrOx film	Open circuit potential measurements at various pH	Not reported	[109]
Pb <sup>2+</sup>	Bismuth thin films	Anodic current peaks from removing accumulated Pb <sup>2+</sup> ions on electrode surface via ASV	50 ppb	[108]
Zn <sup>2+</sup>	Au nanoparticles on SPCE	Stripping current response of analyte during differential pulse ASV	Zn <sup>2+</sup> : 0.05 μg/ L	[172]
Pb <sup>2+</sup>		·	Pb <sup>2+</sup> : 0.02 μg/ L	
Cu <sup>2+</sup>				
As <sup>3+</sup>	MnO <sub>x</sub> on ITO	Stripping current response of As <sup>3+</sup> during LSSV scans	1 ppb	[112]

## Imprinted recognition element

A variation of the RE encapsulation strategy is the use of electropolymerized molecularly imprinted polymers (e-MIPs) as sensors. Instead of simply entrapping the RE, in this strategy, the target molecules themselves are first encapsulated in the electropolymerized layer and then removed to create embedded molecular voids which mimic the shape of the target molecule within and on the surface of the polymer layer [88,89]. In addition to shape, these voids can exhibit chemical (hydrogen bond donors or acceptors) and physical properties (charge and polar-

ity) that are specific to the target molecule. While the molecularly imprinted polymers can also be chemically polymerized, EP offers a finer control of the dimensions of the polymer, a highly intimate contact with the substrate (in some cases the working electrode), a rapid synthesis, and a uniform film morphology [88].

Mulchandani and coworkers [73] described an ion-imprinted polymer (IIP)-modified reduced graphene oxide (rGO) channel as a dual FET/chemiresistor for the detection of Cd<sup>2+</sup> ions in water. Ion imprinting, in this context, is a template-assisted



(a) The conducting polymer composite grown in the organic electrochemical transistor (OECT) channel. An enzyme is physically entrapped within the conducting polymer network. The electropolymerization continues until the source and drain contacts are both covered with the polymer. (b,c) Microscope images showing the growth of p(EDOT-*ran*-EDOTOH):ClO<sub>4</sub> in the OECT channel. (b) (before the bias) and t=2 min (c) The polymerization starts at one gold contact by applying a constant potential at 1 V and continues until the two contacts are bridged by the polymer. (d) Photograph of a four-channel OECT array. The scale bar is 200 mm. (e) Real-time response of the sensor to the additions of uric acid (UA), ascorbic acid (AA), dopamine (Dop) and glucose (Glu) into the measurement solution and to subsequent rinsing with PBS. (f) The response of the four-channel OECT array to  $100 \times 10^{-6}$  M of glucose,  $100 \times 10^{-6}$  M of lactate and  $100 \times 10^{-6}$  M of cholesterol as well as a mixture containing all these metabolites.  $V_G = -0.2$  V and  $V_G = 0$ . Each color represents the response of a channel functionalized with one enzyme alongside the response of bare p(EDOT-*ran*-EDOTOH) channel (green). Reproduced with permission from Ref. [84], copyright 2020 Wiley.

imprinting process applicable to 3D-polymeric networks. Such sensors could achieve a  $LOD_{Cd2+}$  of 2 ppb as well as an excellent selectivity toward Cd(II) over a range of other heavy metal ions.

Moreover, the molecular imprinting technique has also been used to modify the gate electrodes of OECT-based sensing devices. In work from Zhang et al. [90] o-phenylenediamine (oPD) was electropolymerized onto the Au gate electrode, molecularly imprinting ascorbic acid (AA) into the polymer matrix. The rebinding of AA onto the electropolymerized molecularly imprinted polymer layer, in the presence of applied potential on the gate electrode, induced an oxidation current from AA which increased the effective gate voltage and decreased the drain current through the PEDOT:PSS channel. Using a nonconducting polymer largely insulates the electrode, and ideally only allows redox reactions from the binding of the specific electroactive analytes to the film. Other electroactive small molecules could only generate ~ 50 mV change in the effective gate voltage at a higher concentration of 100 μM, compared to the  $\sim 250$  mV change with just 10  $\mu$ M of AA [90].

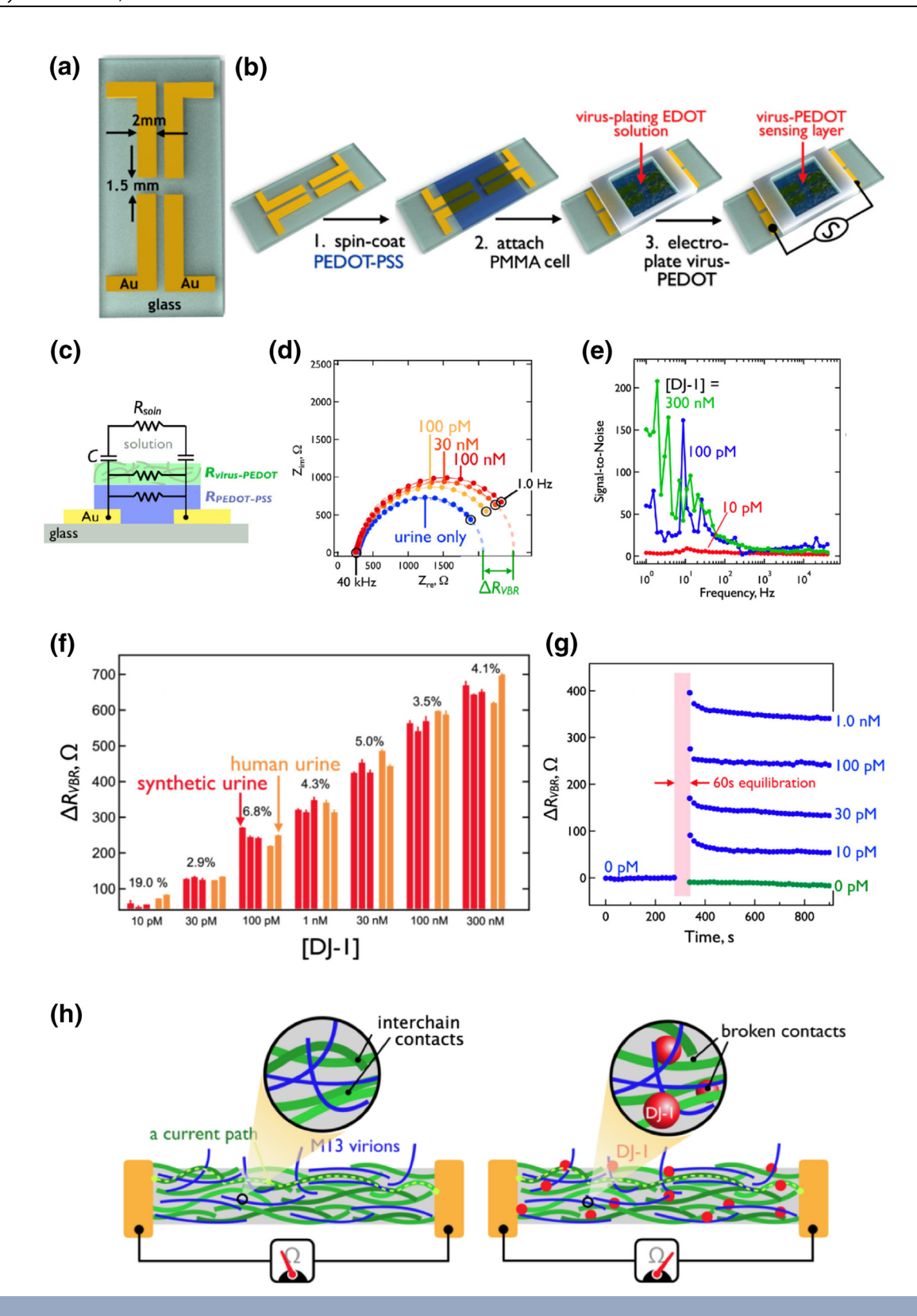
Yang et al. [91] and Wei et al. [92] exploited a similar strategy to create polymeric receptor layers for differential pulse voltammetry (DPV) sensors that respectively target dopamine (DA) and luteolin, a natural pharmaceutical. In these experiments, non-conducting polymers were polymerized onto a conductive electrode while imprinting the target molecule in the polymer

layer. The rebinding of the analyte was detected as an increase in current induced by the electroactivity of the targets. Dehghani *et al.* [93] demonstrated that PANI could be imprinted with cefixime (CEF), a semi-synthetic antibiotic, covering the electrode surface containing graphene oxide and Au nanowires. The PANI-based DPV sensor could successfully be used to detect the CEF based on electrooxidization [93].

#### Surface immobilized recognition element

In addition to entrapping REs (Section "Entrapped/encapsulated recognition elements") and imprinting polymers using the target analyte molecules (Section "Imprinted recognition element"), a third option is to directly attach the RE to the surface. This process can also be facilitated by the EP of suitably modified monomers. Hai et al. [94] used EP to prepare both EDOT and EDOTOA, which is a monomer of EDOT with an oxylamine side chain, to decorate a PEDOT:PSS channel electrode with PEDOT/PEDOTOA in an OECT sensor. The oxylamine groups are introduced due to their covalent attachment chemistry with sialyllactose, which is known to bind human influenza A virus (H1N1). The EP of differently functionalized monomers in thin film morphology simplifies the fabrication of the sensor and ensures good adhesion between the PEDOT:PSS and the PEDOTOA [94].

Wang et al. [95] fabricated a photoelectrochemical sensor by EP of a phenothiazine (PT) monomer, which was synthesized



The Virus BioResistor (VBR). (a) VBRs are constructed on a 10 mm glass chip with patterned Au electrodes. (b) Three processing steps provide for the deposition of a PEDOT-PSS layer by spin-coating from solution (Step 1), the attachment of a PMMA cell (Step 2), and the electrodeposition of a virus-PEDOT layer (Step 3). (c) The electrical response of the VBR is modeled by three parallel resistors and a solution/channel capacitance. (d) This circuit produces a semicircular Nyquist plot for which the high frequency impedance (40 kHz) approximates the solution resistance ( $Z_{re} \approx R_{soln}$ ), and the low frequency impedance is dominated by the parallel resistance imposed of the two film resistors,  $Z_{re} \approx Z_{VBR}$ .  $Z_{VBR}$  increases with the concentration of target protein present in the solution phase. (e) The VBR circuit maximizes signal-to-noise (S/N) at low frequencies, and can exceed 100 at high protein concentrations. Rapid Quantitation of DJ-1 in Urine. (f) Correlation of VBR signal against DJ-1 concentration in urine and synthetic urine. (g) VBR signal *versus* time for the exposure of five VBRs to aliquots of DJ-1 in synthetic urine. (h) Proposed mechanism for VBR signal transduction. Reproduced with the permission of Ref. [48] copyright 2020 American Chemical Society.

to contain a quaternary amine, for the production of a positively-charged polymer that retains the photoelectrochemical properties of poly(phenothiazine) (PPT). Subsequently, negatively-charged CdS quantum dots (QDs) were electrostatically immobilized onto the PPT-based sensing layer. The working principle of signal generation is that acetylcholinesterase (AChE), the active enzyme, will hydrolyze the acetylthiocholine (ATCh) additive and increase the separation distance between the CdS QDs and the sensing body above the threshold to generate sufficient photoelectrochemical current. In the presence of organophosphate pesticides, the enzymatic activity will decrease and the QDs will adsorb to the surface of the polymer, creating sufficient photoelectrochemical current for facilitating the sensing activity.

## Metals, Metal Oxides, and Other Inorganic Materials

While polymeric sensing layers have shown clear strengths in achieving selective sensing of target molecules, they are susceptible to damage in harsh, non-inert environments, limiting their practical scope. In this regard, inorganic materials such as metals or metal oxides show greater physicochemical robustness compared to organics. In this section, we introduce the direct ED and ED-based syntheses of various inorganic materials that support solution-phase sensing. This section is divided into three categories as follows: Noble metals configured as high surface area microelectrodes, Non-noble metals, metal alloys, and metal oxides, and MOFs and MXenes.

#### Noble metals

Au is commonly involved in the fabrication of sensor units due to its biocompatibility, conductivity, compatibility with thiol (S-H) chemistry often used for the self-assembly of organic monolayers, and the facile attachment of REs. ED is not only the most reliable strategy for the fabrication of Au-based sensing layers, but it can also be used for roughening the electrode surface and increasing its electrochemically active surface area as well as the coverage of surface-conjugated RE per unit area [96]. Su et al. [97] investigated the evolution of surface morphology of Au nuclei during Au ED. They observed that, using a constant potential deposition, the size of the Au nanostructures increased with increasing HAuCl<sub>4</sub> concentration and deposition time, but their morphology was potential dependent. Under optimum conditions, highly dispersed flower-like Au nanostructures could be reproducibly obtained. After forming a layer of thiolated ss-DNA on the surface of Au nanostructures through incubation, the product could be used for the detection of a complimentary ss-DNA by measuring the decreases in current associated with the reduction of the redox reporter,  $Ru(NH_3)_6^{3+}$  [97]. Experiments similar to those previously reported by Kelley and coworkers provide additionally relevant case studies [31,33-35].

The research group of Kelley also performed a systematic study of Au morphology as a function of the ED condition [98]. In that study, ED at low overpotentials produced compact, low surface area/volume (SA/V) deposits. With increasing overpotential, spiky structures with high SA/V were formed due to instantaneous nucleation processes followed by diffusion-controlled growth. Conditions favoring the ED of 5-fold twinned needles, which exhibited the highest level of performance for biosensing, were systematically identified.

A number of new applications involving the nanostructured microelectrode systems pioneered by Kelley and coworkers have been described since 2017, including the use of electrodeposited nanostructured gold microelectrodes (Fig. 5a) for highly specific gene-circuit based DPV sensors (Fig. 5b). The high surface area of these electrodes allowed for dense functionalization of the surface using thiolated DNA, followed by large faradaic currents after the binding of the complimentary DNA which was labeled with methylene blue, a redox active reporter molecule.

Peng et al. [100] used a similar strategy to modify the gate electrode in their OECT device. The Au gate electrode decorated with Au nanoparticle by ED was incubated with thiolated DNA capture probe. The binding of the analyte to the RE on the gate electrode causes a decrease in the drain-source current through the PEDOT:PSS channel, due to the voltage drop between the gate and the solution. The authors determined that ED of Au nanoparticles on the smooth Au electrode greatly improved the signal, likely by increasing the number of probes and thus the amount of microRNA which was on the surface of the gate electrode. Other attempts at using Au nanoparticle ED for DNA based sensing have been widely reported [101–104].

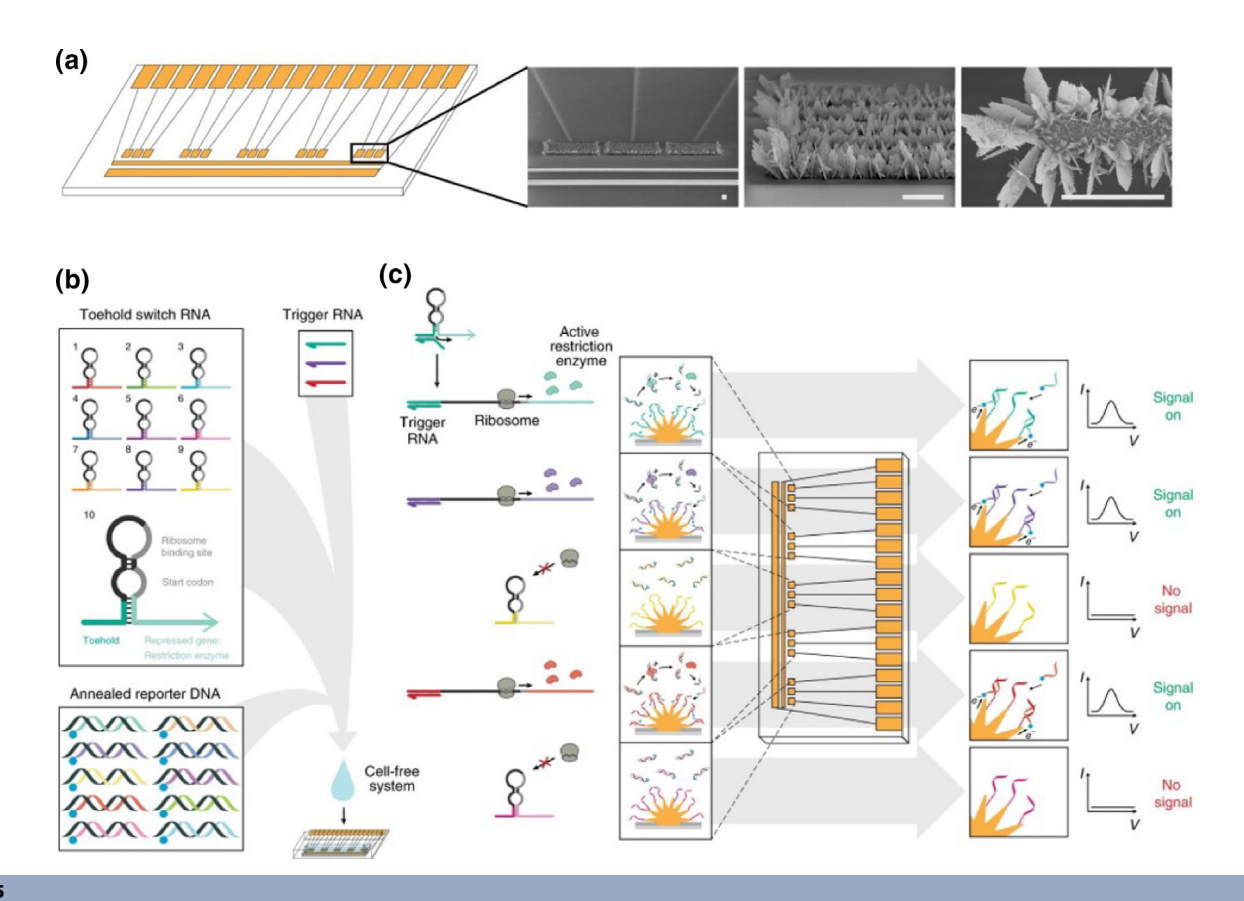
Other than Au nanoparticles, Au nanotubes have also been employed as high SA/V Au electrodes for DNA sensing. Work done by Shariati *et al.* [105] used porous polycarbonate as a vertical template for Au EP. Thiolated DNA capture probes are then immobilized onto the Au nanotubes, which were then analyzed using electric impedance spectroscopy (EIS) and a redox couple.

In addition to Au, other noble metals can be electrodeposited and roughened in a similar manner. Pd, for example, has been electrodeposited in a high surface area nanoflower formation to make an FET-style glucose sensor [106]. They report that lower sulfuric acid concentrations lead to sharper dendrites, which improve the signals upon glucose oxidation. By electrodepositing Pt and Pd onto a porous GaN template, Xi *et al.* [107] were able to create a bimetallic nitrite sensor. A synergistic effect between the GaN template and the Pd-Pt bimetallic nanoparticles was found to enhance the speed of the nitrite electrocatalysis, and the controllable porosity of the GaN further enhanced the speed of this device. The deliberate choice of this electrode material is both chemically and structurally beneficial to the device's design, and future sensors could benefit from similar innovation.

## Other metals and metal oxides

To optimize the lead-sensing capabilities of bismuth films, Rajamani *et al.* [108] produced a variety of different morphologies using ED. Additives such as citric acid, polyvinyl alcohol, and betanine created distinct surface structures, and pulsed ED further refined the bismuth surface. Structures ranging from hexagonal nanorods to urchin-like polyps were fabricated, each with different surface enhancement characteristics, and they were tested for sensitivity towards lead ions. The presence of additives served as a simple way to control the morphology of electrodeposited metal films to optimize their sensing performance toward electrochemically active aqueous ions.

Zea *et al.* [109] modified inkjet-printed Pt electrodes by ED of iridium oxide to create a two-electrode lab-on-a-chip device. The inkjet printing method combined with electrochemical modifi-



(a) ED of nanostructured Au electrodes for multi-channel sensors. Scale bars are 50 µm, (b,c) A gene-circuit/electrode interface for cell-free synthetic gene networks. By combining cell-free transcription and translation systems with engineered gene circuits on nanostructured microelectrodes, distinct and multiplexed output signals can be tracked in parallel. This approach uses toehold switch-based RNA sensors, which, in the presence of trigger RNA, express one of ten restriction-enzyme-based reporters. Upon sensor activation, expressed restriction enzymes cleave annealed reporter DNA, which is free floating in cell-free reactions, releasing reporter DNA labelled with the redox reporter (blue circle). Nanostructured microelectrodes with conjugated capture DNA then recruit the redox-active reporter DNA to their surface, generating an electrochemical signal. Each toehold switch is engineered to produce a unique restriction-enzyme-based reporter that is coupled to a distinct reporter DNA and capture DNA pair for multiplexed signaling. Reproduced with the permission of Ref. [99], copyright 2020 Nature Publishing.

cation allows researchers to cut the cost on high surface area electrodes, which are typically expensive to prepare. By measuring the open circuit potential (OCP) versus an integrated Ag/AgCl electrode, the authors resolved a highly linear response across pH 3–10. Combining ED of iridium oxide with inkjet metal printing means this sensing platform can be used in applications involving low impedance, such as neural recordings, and can be applied to a variety of different metals and metal oxides.

ED can also be used to create alloyed nanostructures. An electrodeposited Pt-Cu alloy could be used electrocatalytically to detect methanol, a harmful substance that is toxic by consumption, in different food samples [110]. Additionally, Naik *et al.* [111] demonstrated electrodeposited NiCo<sub>2</sub>O<sub>4</sub> – Pd nanosheets which were used for the electrocatalytic detection of glucose.

Metal oxides can also be deposited to create high surface area sensors. Gupte  $et\ al.\ [112]$  were able to deposit roughened  $MnO_x$  onto ITO, and by varying the deposition conditions, created morphologies that ranged from sea urchin-like spheres, nanorods, and flakes. Using linear sweep stripping voltammetry (LSSV), the authors were able to reversibly reduce and oxidize  $As^{3+}$  onto the  $MnO_x$  surface, creating an electrochemical sensing

response to the heavy metal. The selective deposition of  $\mathrm{MnO_x}$  enables selective sensing of  $\mathrm{As^{3+}}$  over other heavy metals for a low cost in comparison to other methods.

#### MOFs and MXenes

Metal organic frameworks (MOFs) have received attention as templates for various sensing applications due to their tunable porosity, large surface area, well-defined crystal structures, and versatility. Recently, the ED of multiple MOFs onto electrodes for both electrochemiluminescence (ECL) [113] and DPV [114] immunoassays have been reported. These authors electrodeposited both Ru(bpy)<sub>3</sub><sup>2+</sup>-functionalized MOFs (Ru-MOF) and hemin-based MOFs as thin films to perform their sensing. They report that the electrogeneration of OH- from the constant applied potential in the cell deprotonates the ligands and aids in the formation of the MOF, while also encapsulating the Ru  $(bpy)_3^{2+}$ . The growth of the MOF crystals at the electrode surface closely adheres the MOF layer to the electrode surface. Chitosan and glutaraldehyde, which serve as the RE, are then drop coated onto the electrode and dried. This functionalization provides a means for antibodies to be covalently bound to the surface.

The introduction of the protein, which the antibody exhibits a specific binding to, causes a decrease in the ECL intensity. In the case of the hemin-based MOFs, the MOF thin film was a template for ED of Pt nanoparticles that facilitate the interaction between the thiol and the antibodies. The current during DPV signal was generated from the electroreduction of oxygen (oxygen reduction reaction; ORR) in the solution, which decreased as the antibody bound to the surface. This is due to the hemin moieties which have excellent electrocatalytic performance towards the ORR.

Electrophoretic deposition has also been used to create functionalized electrode surfaces. Sharifuzzaman et al. [115] demonstrated the ED of MXenes onto microfabricated Au electrodes for use as biosensors. Here, MXenes refer to multilavered transition metal nitrides with chemical formula  $M_{n+1}X_nT_x$ , where M are transition metals, X are C and/or N, and Tx. The electrophoretic process developed by the authors, specifically termed "electroMXenition," could successfully generate 2D MXene nanosheets (MXNS) (Fig. 6a). A range of MXNS coverages could be obtained by appropriately tuning the experimental parameters (Fig. 6b). Nuclear matrix protein 22 (NMP-22) and apolipoprotein A1 (Apo-A1), the target analytes in this study, are protein biomarkers expressed in urine for bladder cancer. To enable their selective detection, anti-NMP-22 and anti-Apo-A1 antibodies were conjugated to the MXNS layer formed by electroMXenition. As a result, DPV of an outer-sphere redox couple in solution produced current peaks that were attenuated as the concentration of (blocking) NMP-22 and Apo-A1 were increased, showing the transduction capabilities of the MXNS (Fig. 6c and d).

#### Future outlook

EP and ED have been exploited to create various types of materials for quantitatively detecting different analytes in aqueous solutions and bodily fluids. EP provides a fast, reliable, and reproducible method of coupling receptor molecules with the polymer layer or imprinting the target in the polymer. On the other hand, ED allows for nanostructuring of metallic surfaces, synthesis of metal alloys, controlled electrophoretic deposition of nonmetallic inorganics (*e.g.*, MOFs and MXenes), and other complex processes.

However, many of these sensors require redox couples and interfacial potential control provided by external electrodes in order to generate the signal, which increases the design complexity. For point-of-care applications, where simplicity of operation is critically important, the added complexity is a disadvantage. Therefore, we should prioritize the research and development of biosensor architectures that exhibit sufficient sensitivities without added redox species.

A promising solution can be found in organic electrochemical transistors (OECTs) operating in a three-terminal mode with the monolithic source, the drain, and the external or internal gate electrodes. Over the last decade, considerable efforts have been undertaken to provide the essential fundamental understanding of the functionalities of OECTs devices under varying conditions of solution composition [116].

#### **Gas Sensors**

Gas sensors, in contrast to solution-phase sensors or biosensors, are most often designed as two terminal chemiresistors that pro-

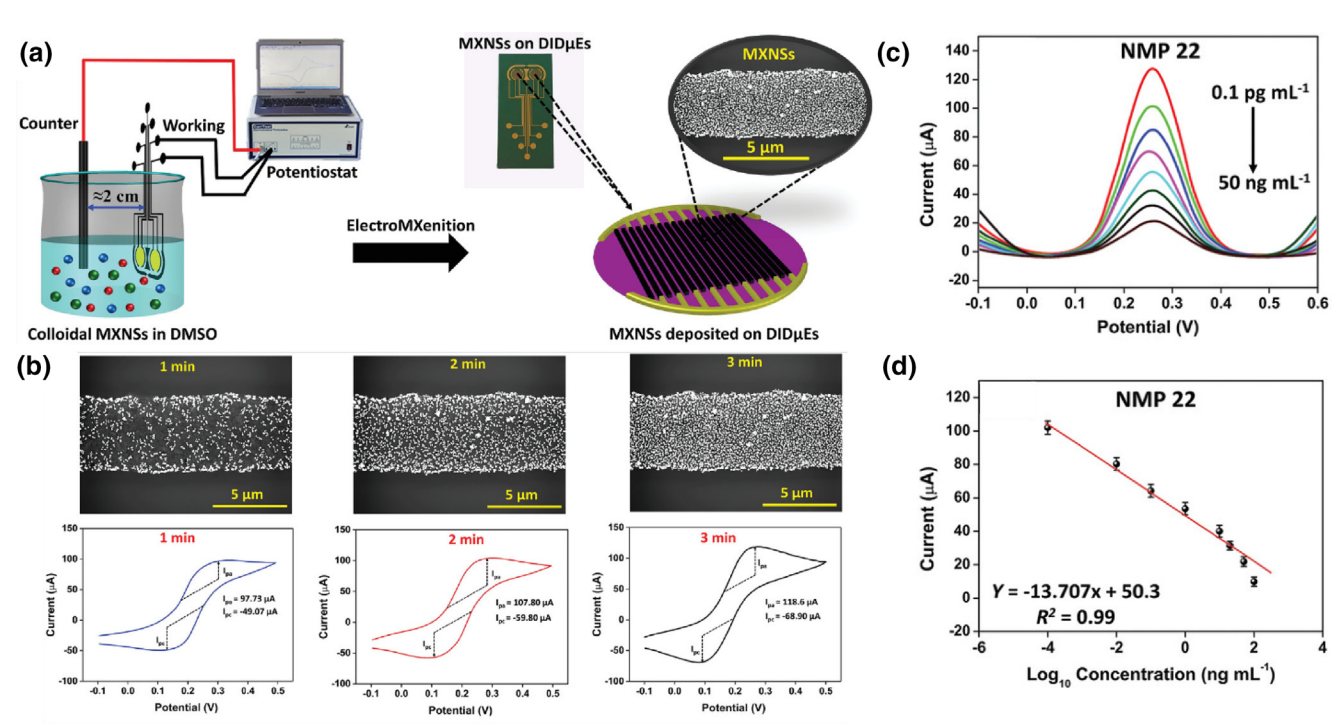


## FIGURE 6

(a) Schematic illustration of the customized electrolyte bath and the "electroMXenition" process. (b) Uniformity and redox performance analysis of the MXNSs onto DIDµEs at room temperature using FESEM and CV (in 5 mM K3/K4 solution) under different electroMXenition times (1–3 min), with optimized concentration and constant voltage. (c) DPV response for NMP 22 detection at different concentrations showing the decrease of the observed peak current with increasing NMP-22 concentration. (d) The resulting calibration plot for NMP-22. Reproduced with the permission of Ref. [115], copyright 2020 Wiley.

duce a resistance change upon exposure to a target gas [12,117–121]. Similar to the previous section, the various classes of materials are based on different sensing mechanisms, so it is helpful to understand the advancements in electrodeposited gas sensing elements with respect to each materials class. This section discusses sensing layers based on carbons (Section "Carbon transducers"), conductive polymers (Section "Electronically conductive polymers"), metal oxides (Section "Metal oxides"), and metals (Section "Metals"). A brief summary of gas sensing metrics and gas sensors enabled by ED are found in Table 3 and 4, respectively.

#### Carbon transducers

The preponderance of new developments in this category has involved carbon nanotubes (CNTs), graphene (including rGO), and carbonized polymeric (e.g., polyacrylonitrile) nanofibers.

Carbon nanotubes were one of the first low-dimensional materials used for gas sensing, as described in the pioneering work by Zettl *et al.* [122] in which it was discovered that the resistance of CNTs could be modulated by O<sub>2</sub> with high sensitivity.

TABLE 3
Allowable concentration limits for relevant gases (source: OSHA, 2022).

Analyte	Relevant Required Limits	Ref.
NH <sub>3</sub> (g)	50 ppb – Medical	[173]
	1 ppm – Environmental	
C <sub>2</sub> H <sub>5</sub> OH (v)	100 ppm/hr, 0.26 ppm	[174]
	(Matching OSHA 5001 limits)	
$H_2S$ (g)	2.5 ppm/hr (USA)	[175]
	6.6 ppm (China)	
$NO_2$ (g)	5 ppm (OSHA)	[176]
H <sub>2</sub> (g)	Explosive 4–74%	[177]
HCN (g)	1.25 ppm/hr, 4.7 ppm	[178]

Since then, there have been thousands of papers describing the application of modified CNTs as chemiresistors for gas sensing (recent reviews are: [123–125]). In the perspective of practical viability, however, the performance of carbon-based materials can be further improved through the decoration of sensitizers (*e.g.*, noble metal catalysts), which can be effectively conducted through ED.

In this manner, chemiresistive H<sub>2</sub> sensors have been achieved by decorating CNTs with Pd and Pt nanostructures through ED approaches. A persistent problem in conventional H<sub>2</sub> sensors has been the slow response times, which have been up to several minutes. In a practical setting, the sensor fails to produce an invariant, steady-state resistance changes upon exposure to H<sub>2</sub> within a reasonable window of time (ideally, within a minute). Li et al. [126] assessed that the size of the deposited Pd or Pt particles had not been tightly controlled in prior studies, and that these particles were also too large - often in the micron-scale. Pulsed ED methods provide the means for preparing a high density of noble metal nanoparticles that also narrowly distributed in diameter [127]. Using such methods, lithographically patterned carbon nanotube ropes (Fig. 7a and b) were decorated with Pd nanoparticles with mean diameters in the range of 4.5to 6-nm (Fig. 7c-e). The resulting sensor performance was comparable to that of single Pd nanowires, but CNT@PdNP H2 sensors were both faster and more sensitive with an LOD in the 10 ppm range at room temperature in air [126].

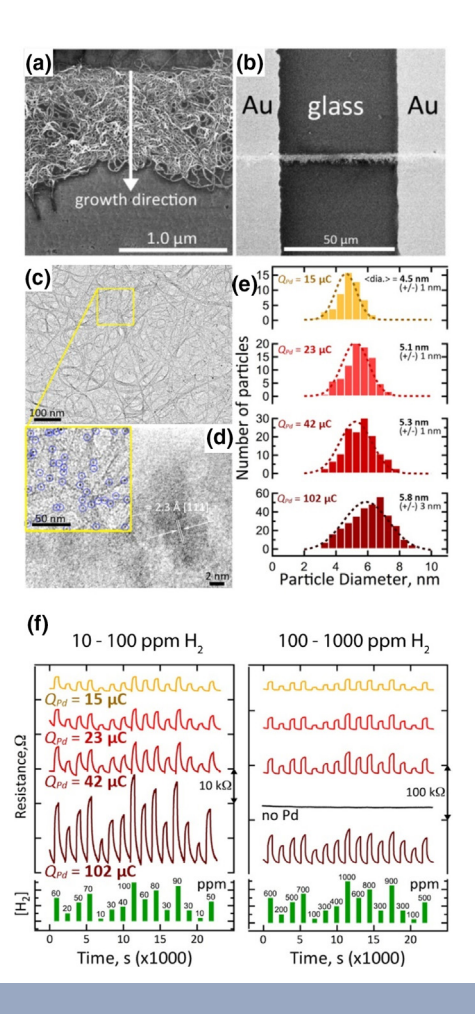
## Electronically conductive polymers

Using the galvanostatic ED of polypyrrole films, Nekrasov and coworkers [128] produced a polymeric ammonia sensor. The reductive influence of the ammonia allowed for oxidation on the PPY film, which impacted the conductivity of the film. The

Gas sensors enabled by ED

TABLE 4

Analyte	Electrodeposited Material	Detection Modality	Limit-of- Detection	Ref.
C₂H₅OH (v)	Flower like ZnO EDed on GaN	Resistivity across the ZnO-GaN heterostructure	100 ppb	[132]
$C_2H_5OH$ (v)	ZnO EDed films on ceramic	Resistivity across ZnO film	>1000 ppb	[133]
$NH_3$ (g)	Galvanostatic ED of polypyrrole	Resistivity across polypyrrole thin films	>2 ppm	[128]
H <sub>2</sub> S (g)	Dielectrophoretic deposition of sc-SWCNT	Relative resistivity values on sc-SWCNT@AuNP working electrodes	3 ppb	[179]
$NH_3$ (g)	PANI-PSS@TiO₂NP ED	FET-Ion selective gate electrochemical response	50 ppt	[130]
$NO_2$ (g)	WO <sub>3</sub> films onto porous silicon	Relative resistivity measurements across WO <sub>3</sub> @PS films	$\sim$ 50 ppb	[180]
NH <sub>3</sub> (g)	PDMA/PANI films EDed onto ITO electrodes	Conductometric sensor based on double lateral heterojunction, PDMA@LuPc $_2$	320 ppb	[129]
$H_2$ (g)	Lithographically patterned PdNW ED	Relative resistivity values on PdO NW sites	10 ppm	[131]
$H_2S$ (g)	ZnO NR ED on GaN	Relative resistivity values on $Al_2O_3$ @GaN@ZnO-NR composite	1 ppm	[175]
H <sub>2</sub> (g)	Cauliflower-like Pt-black nanoflowers	Thermocatalytic $H_2$ sensor based on relative resistivity values	75 ppm	[181]
$NO_x$ (g)	Ni deposition onto as prepared porous ZnO	Relative resistivity on Ni@ZnO composite	1 ppm	[182]
H <sub>2</sub> (g)	PtV on PCNWLs	Catalytic $H_2$ sensor based on relative resistivity measurements	>10 ppm	[183]
$H_2S$ (g)	Ordered Cu-ZnO nanorods (NRs) on quartz crystal microbalance (QCM) oscillators	Measured by piezoelectric frequency shifts of the QCM crystal	79 ppb	[184]
HCN (g)	Ordered Cu-ZnO NRs on QCM oscillators	Measured by piezoelectric frequency shifts of the QCM crystal	169 ppb	[184]



H<sub>2</sub> sensors based upon carbon nanotube (CNT) ropes decorated with Pt nanoparticles. (a) A section of CNT rope 1.0-1.5 μm in width. (b) A Pd-CNT rope H<sub>2</sub> sensor consisting of a single CNT rope decorated with Pd nanoparticles (not visible in this image) and evaporated Au electrical contacts. (c) Low-magnification TEM image of a CNT rope after the deposition of Pd nanoparticles ( $Q_{Pd}$  = 42  $\mu$ C). Pd nanoparticles are distributed across this entire image, with some of the largest seen as dark spots in the lower right corner of this image. (d) (Inset) Higher magnification view of the region shown in yellow in (i). Blue circles highlight ~40 Pd nanoparticles present in this region. (d) A high-resolution TEM image of one of these nanoparticles is shown in the main image. (e) Histograms of Pd nanoparticle diameters obtained from TEM analysis at the indicated  $Q_{Pd}$ . (f) CNT@PdNP H<sub>2</sub> sensor responses, for devices prepared using four Q<sub>Pd</sub> values, as indicated. H<sub>2</sub> sensing data for two [H<sub>2</sub>] concentration ranges. Reproduced with the permission of Ref. [126], copyright 2017, the American Chemical Society.

conductivity was directly influenced in correlation with the concentration of ammonia within the system [128]. In humid environments, detection became much less convenient due to the conflicting influence of water molecules on the properties of the PPY layer, but robustness of the sensor against high humidity is often required for any realistic applications. Mateos *et al.* [129], demonstrated sensing in a humid atmosphere using electropolymerized poly(2,5-dimethoxyaniline) (PDMA) in a double lateral heterojunction FET. The authors performed EP and deposited the PDMA species on the ITO electrode and a lutetium bisphthalocyanine (LuPc<sub>2</sub>) layer was placed on the PDMA. The authors demonstrate that, since the conductivity of the PDMA layer is

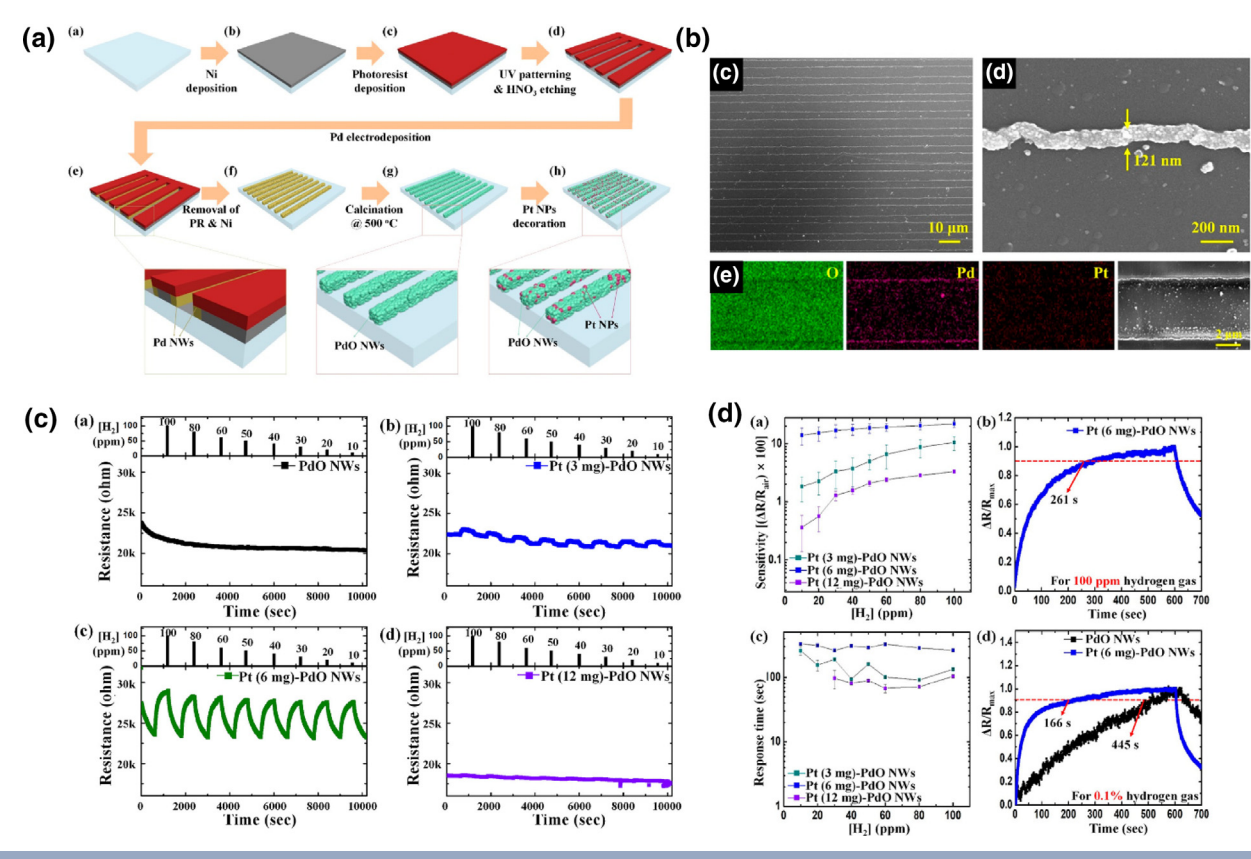
governed by positive charge carriers that are generated upon interaction with  $\mathrm{NH}_3$ , the change in current directly correlates to the  $\mathrm{NH}_3$  concentration. Since humidity does not impact these charge carriers in any significant manner, the sensor is reliable across 10–70% relative humidity values [129]. The lowest limit of detection demonstrated for ammonia sensor in the selected literature was 50 ppt achieved using  $\mathrm{TiO}_2$  nanoparticles electrodeposited on PANI-PSS [130]. The high negative surface charge density on the  $\mathrm{TiO}_2$  nanoparticles allowed for efficient binding of  $\mathrm{NH}_4^+$  and the oxygen atoms in the nanoparticle will promote the formation of hydrogen bonds with the analyte. Indeed, this bonding causes a shift in the resistivity of the PANI-PSS/ $\mathrm{TiO}_2$  layer, facilitating the detection of ammonia [130].

## Metal oxides

Cho *et al.* [131] discuss the fabrication of PdO nanowires by an indirect approach which involved the initial synthesis of Pd nanowires by the aforementioned LPNE method of ED, followed by calcination at 500 °C for the conversion of Pd into PdO (Fig. 8a). Through this simple two-part strategy, a highly aligned array of PdO nanowires could be obtained (Fig. 8b). Even though the PdO nanowires could not function as H<sub>2</sub> sensors on their own due to low responses and sluggish response times, the authors discovered that simply decorating the PdO nanowires with an optimal amount (6 mg) of Pt catalysts helped unlock their potential for rapid and linear chemiresistive responses to H<sub>2</sub> at room temperature (Fig. 8c and d).

Wang et al. [132] provide a case study on the use of electrodeposited metal oxides for the determination of volatilized ethanol. The authors utilized ED to prepare flower-like ZnO on GaN semiconducting substrate. Electrical transduction occurs when ethanol adsorbs on the surfaces of porous ZnO structures through interaction between the O<sup>-</sup> and the ethanol molecules (Fig. 9ac). This led to a decrease in the work function of ZnO, modulating its electronic structure. The authors reported the stability of the sensor over five cycles with response and recovery times of 12 and 9 seconds, respectively [132]. Pan et al. [133] employed an identical mechanism with macroporous ZnO structures electrodeposited on a rGO/Au-coated ceramic tube. Stability of this sensor was tested for over 50 cycles with response and recovery times of 12 and 8 seconds, respectively [133]. In both cases, the oxidation of ethanol on the ZnO surfaces generate free electrons that influence the electrochemical response [132,133]. The resulting limits of detection of these sensors are in the 0.1-1 ppm range, which is suitable for environmental monitoring.

Several other examples of electrodeposited metal oxides for use in gas sensing can be found in the literature as well. Zhang et al. [134] demonstrated the hierarchical rose-like nanostructures of NiO produced by ED, in which well-connected nanosheet structure facilitates effective charge transport while the high surface area promotes more surface interaction with the ethanol target gas, resulting in improved sensing performances. (Fig. 9d-f) Also, Poongodi et al. [135] WO<sub>3</sub> nanoflakes with a vertical orientation using template-free ED in a peroxotungstic acid solution, which exhibited a dual-functionality of electrochromic and chemiresistive responses toward H<sub>2</sub>S gas (Fig. 9g-i).



Pt nanoparticle-decorated PdO nanowires for H<sub>2</sub> Sensors. (a) Process flow for the preparation, using Lithographically Patterned Nanowire Electrodeposition (LPNE) of PdO nanowires. In the final step, Pt nanoparticles are deposited on the PdO nanowires using an electroless deposition process. (B) (i) Arrays of Pt-decorated PdO nanowires. (ii) a single such nanowire and, (iii) EDS elemental analysis for oxygen, Pd and Pt. (c) Response of several sensors to hydrogen gas, revealing the importance of the Pt nanoparticles which impart sensitivity to H<sub>2</sub>. (d) An optimal Pt loading near 6 mg is observed in these experiments. Excess Pt beyond this optimum value reduces sensitivity to H<sub>2</sub>. Reproduced with the permission of Ref. [131], copyright 2018 the American Chemical Society.

#### Metals

Jang *et al.* [136] described the preparation of hollow Ag/Pd alloy nanowires, which was achieved by carrying out the galvanic replacement of lithographically patterned Ag nanowires upon exposure to Pd<sup>2+</sup> solutions. When the reaction was carried out for an optimum period of 17 h, Ag nanowires were transformed into Pd@Ag hollow nanowires that showed enhanced H<sub>2</sub> response and accelerated sensing response times, which was reduced 2.5-fold compared with Ag nanowires. Arrays of these Pd@Ag hollow nanowires were deposited onto colorless and flexible polyimide films, resulting in a robust and flexible hydrogen sensing system.

There are several examples since 2001 regarding electrode-posited Pd and Pt nanowires, in particular, for the detection of hydrogen gas [118,138]. An advance in Pd nanowire-based  $\rm H_2$  sensing was achieved by Koo *et al.* [137] in 2017 by the application of a nanofiltration layer to interface with the electrode-posited metal nanowire array, improving the performance of the sensor (Fig. 10). The nanofiltration layer consists of Zn-based metal organic frameworks (zeolitic imidazolate framework 8; ZIF-8), which were deposited onto the lithographically patterned Pd nanowires. The ZIF-8 layer possesses several micropores with an average size of 3.4 Å, which allows for the predominantly selective penetration of hydrogen molecules. Because the kinetic diameter of  $\rm H_2$  (2.89 Å) is smaller than the

pore size, whereas typical interfering gas molecules including oxygen (3.45 Å) and nitrogen (3.64 Å) in air are larger, the interfering species are effectively screened out. The major influence of this engineered nanofiltration layer was the acceleration of response speeds, both the response and the recovery, by a factor of about 20. This effect is attributed to the elimination of surface-adsorbed oxygen and its derivatives (OH and  $\rm H_2O$ ) on the Pd surface, which otherwise blocks the reactive Pd sites [137].

#### **Wearable sensors**

Wearable sensors refer to a sensing device that can effectively interface with the human body to monitor various physiological changes and provides critical information that are necessary for the development of point-of-care diagnostics. Unlike the previous sections, which discussed different types of sensors each with their unique transduction mechanisms, practical wearable devices consist of several dissimilar sensors in a single array. Herein, we separately discuss the two main categories of sensors used in wearable electronics: physical sensing devices (Section "Physical sensors") and chemical sensing devices (Section "Chemical sensors"). Physical sensing refers primarily to strain and temperature sensing, and chemical sensing refers to the detection of biomarkers found in bodily fluids, most often in perspiration. A brief summary of wearable sensors enabled by EP and ED are found in Table 5.

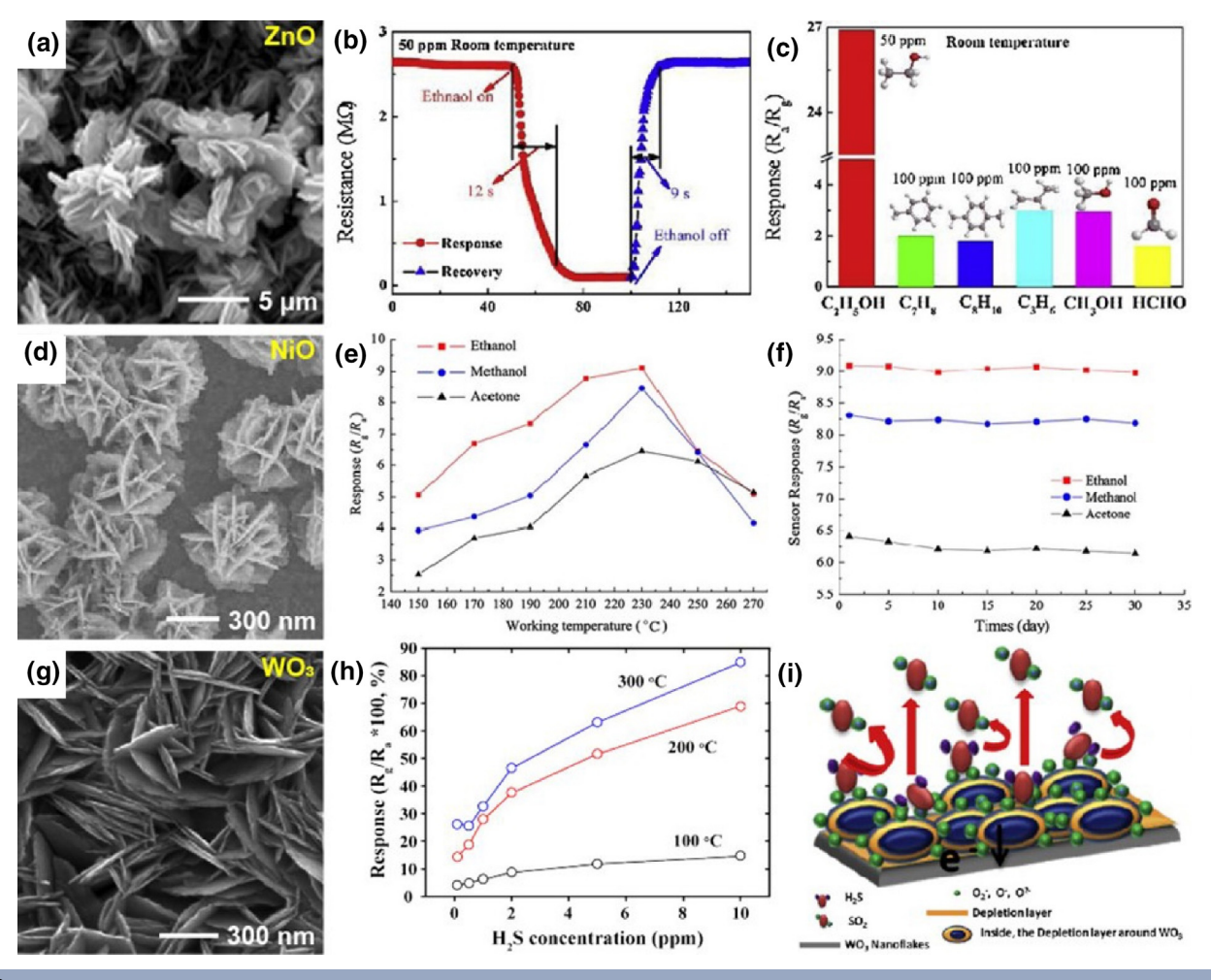


FIGURE 9

Electrodeposited metal oxides for gas sensing applications. (a-c) Flower-like ZnO nanostructures assembled on GaN substrate. (a) SEM image of the ZnO nanostructures. (b) Change in resistance of the ZnO nanostructures upon exposure to 50 ppm ethanol, showing fast response and recovery rates. (c) Selectivity of the ZnO nanostructures to ethanol. Reproduced with the permission of Ref. [132], copyright 2019 Elsevier. (d-f) Rose-like NiO nanostructures prepared by ED. (d) SEM image of the NiO nanostructures. (e) Chemiresistive response of NiO toward ethanol, methanol, and acetone over ranges of working temperatures. (f) Stability of the chemiresistive responses. Reproduced with the permission of Ref. [134], copyright 2016 Springer Nature. (g-i) Vertically-oriented WO<sub>3</sub> nanoflakes prepared by template-free ED process. (g) SEM image of WO<sub>3</sub> nanoflakes. (h) Chemiresistive response of WO<sub>3</sub> toward H<sub>2</sub>S at different concentrations and operating temperatures. (i) Proposed mechanism for the sensing of H<sub>2</sub>S, which reacts with pre-adsorbed oxygens to shrink the depletion layer. Reprinted with the permission of Ref. [135], copyright 2017 Elsevier.

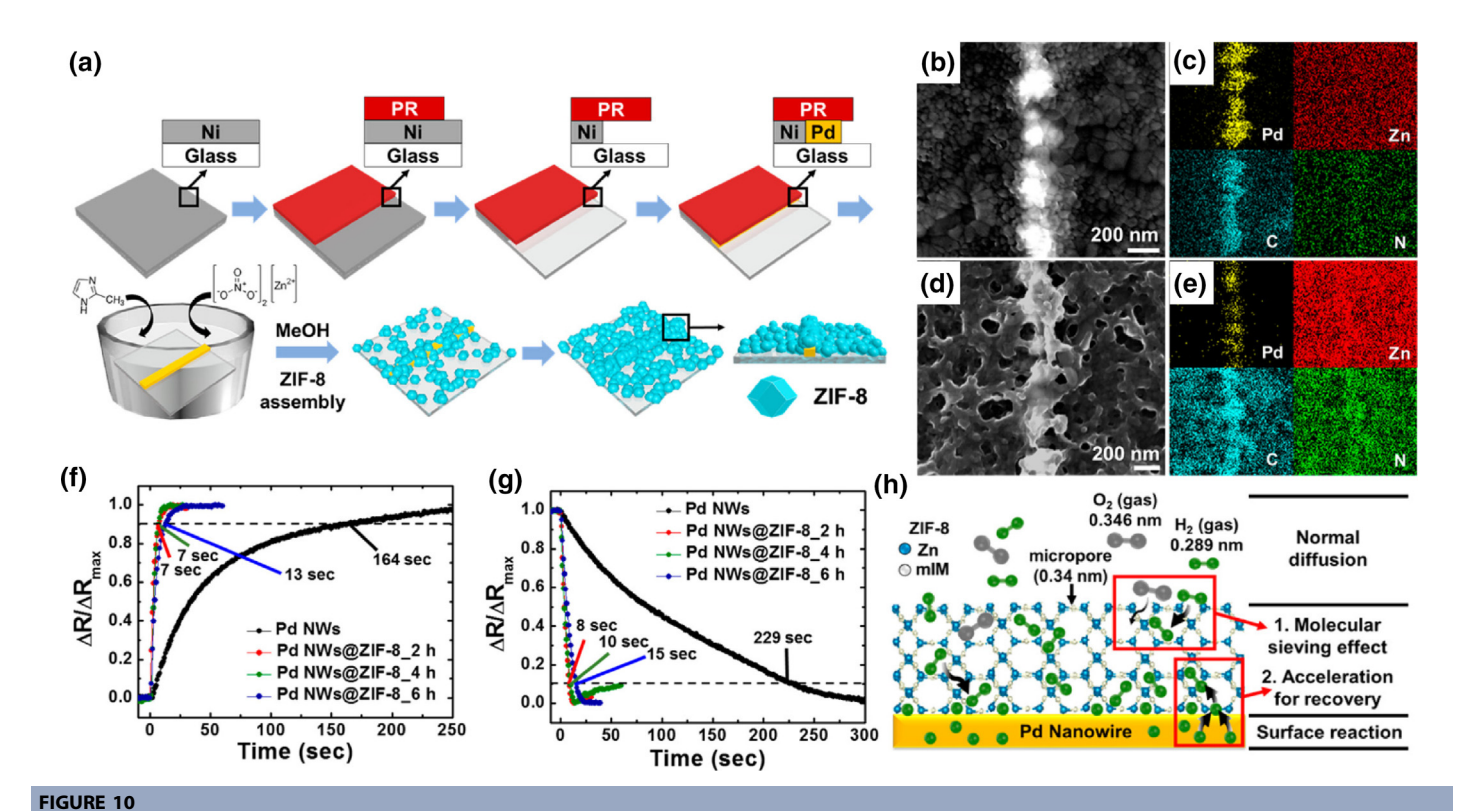
## Physical sensors

Wang and coworkers [139] fabricated a flexible, thin film temperature sensor primarily composted of natural silk nanofibers subjected to thermal carbonization (600 °C) followed by the ED of Pt nanoparticles onto these fibrous carbon networks. Such films produced a linear decrease in resistance as the temperature was increased from of 35.6 °C to 63.6 °C and retained the ability to measure temperature upon bending of the film [139].

Strain sensors have also exploited electrodeposited materials. Dahiya and coworkers [140] prepared a PEDOT:PSS/MnO $_{\rm x}/$  PEDOT:PSS sandwich thin film structure in which the MnO $_{\rm x}$  layer was electrodeposited. In more detail, Lycra elastane fiber fabrics were coated with PEDOT-PSS that was doped with 5% dimethyl sulfoxide (DMSO). MnO $_{\rm x}$  was EDed from an aqueous solution of 0.1 M manganese acetate. A second layer of PEDOT-PSS was then solution deposited. The application of strain to such 3-layer films produced a decrease in the measured

film capacitance by 15% for an applied strain of 40%. An application for such strain sensors involves the real time monitoring of respiratory action (inhale/exhale cycles) [140].

A multifunctional pressure, thermal, and proximity sensor has been described by Jo *et al.* [142]. These devices employed electrospun polyacrylonitrile nanofibers that are decorated with platinum nanoparticles to confer electrical conductivity, and then coated with a conformal electroplated nickel layer [142]. Further, He *et al.* [143], produced a Ni@MnO<sub>2</sub>//Zn microbattery capable of onboard energy storage and strain sensing. In this example, nanoporous 3D Ni skeleton structures were formed by ED on the surface of carbon nanotube films (CNTF). Therein, CNTF@Ni is used as the working electrode in a solution of MnSO<sub>4</sub> to facilitate decoration of the MnO<sub>2</sub>. Zn nanosheets are also deposited in a similar fashion. The strain sensing performances of these systems were verified using strain correlated current measurements [143].



(a) Schematic description of synthesis of Pd NWs@ZIF-8 using LPNE associated with ZIF-8 assembly process. PR is photo resistor and MeOH is methanol. (b-e) SEM and EDS elemental images of Pd NWs@ZIF-8 with growth time of 4 h (b,c) and 6 h (d,e). (f-g) Normalized curves of response (f) and recovery (g) for Pd NWs and Pd NWs@ZIF-8 with different growth time. Growth time is indexed as  $\times$  h. (H) Scheme of accelerated H<sub>2</sub> gas sensing performance of Pd NWs@ZIF-8. ZIF-8 overlayer facilitates selective diffusion of H<sub>2</sub> gas but retards diffusion of O<sub>2</sub> gas, improving recovery and response properties. Reproduced with the permission of Ref. [137], copyright 2017, the American Chemical Society.

## Chemical sensors

Sweat sensors

Human sweat contains several biological reporter molecules that can be used to monitor a person's physiological health. For example, elevated lactate levels in sweat can be indicative of numerous illnesses including: heart failure, circulatory/respiratory issues (leading to an oxygen deficit), metabolic disorders, and renal failure [144]. Further, glucose variance can easily be linked to diabetes, making real-time measurements of paramount importance. Wearable sensors enable non-invasive, reliable monitoring of such biomarkers, allowing healthcare professional and patients to easily monitor the progression and prognosis of diseases.

Wang et al. [145] developed elastomeric textiles for lactate monitoring using Au fibers prepared using ED, integrated with several active components including Prussian blue, LO<sub>x</sub>, and chitosan. The working electrode was prepared by deposition of Prussian blue via a cyclic voltammetry (CV) method. The chitosan and LO<sub>x</sub> are drop-cast onto the electrode to fabricate the composite. The wearable reference electrodes were prepared using another CV-based deposition method, Ag is deposited onto the elastomeric Au fiber and then coated with polyvinyl butyral (PVB) for stability. The authors achieve a LOD of 0.137 mM in a phosphate-buffered saline for lactate and remains physiologically relevant in an artificial sweat matrix [145]. Separately, glucose determination with cloth textiles was achieved by Peng et al. [146] using electrodeposited cotton-like gold microspheres

(CGM), which supports redox activity on its surface, resulting in an impressive sensing selectivity toward glucose with a limit of detection of 0.78  $\mu M.$ 

Bariya *et al.* [147] developed an ED-based textile sensor compatible with sweat, urine, and saliva for the multiplexed detection of glucose, caffeine, Na<sup>+</sup>, K<sup>+</sup>, and Cu<sup>2+</sup>. Electrochemical deposition in this case is used both for preparing the electrochemical sensing layers as well as for detecting the ions. Electrode functionalization was performed using CV for PANI and Prussian blue, while galvanostatic EP process was used for PEDOT:PSS [147]. Therein, the hydrogel-based glucose detection matrix, containing the  $GO_x$  enzyme, is used as the primary sensing layer for the enzymatic detection of glucose, transduced in combination with Prussian blue. The electrodeposited PANI was responsible for the determination of pH as a function of voltage in the sweat matrix. The determination of Na<sup>+</sup>, K<sup>+</sup> and Cu<sup>2+</sup> were performed using ion-selective membranes, made possible by an ion-to-electron transduction film interface [147].

Calcium ions are another useful physiological marker as a cofactor in biological catalysis and an endogenous messenger signal. Using a carbon working electrode, Au nanoparticles were electrodeposited onto the surface using the CV deposition method in a  $HAuCl_4$  solution, followed by the ED of rGO. The rGO acts as an asymmetric capacitor which, when in contact with the electrolyte, will change its capacitance. An ion selective membrane is placed on the rGO surface to exclude any interfering analytes, isolating just the  $Ca^{2+}$  for their selective detection [148].

Heavy metals are of significant concern in many facets of environmental analytical chemistry [149]. Bismuth is an optimal choice for a working electrode for heavy metal ion anodic stripping voltammetry due to its ability to form amalgamations with various heavy metals, as well as its facile ED and nanostructures [150]. One example of a wearable heavy metal sensor is the Zn<sup>2+</sup> sensor presented by Xuan *et al.* [149] who electrodeposited bismuth onto a composite of polydimethylsiloxane (PMDS) and laser-induced graphene (LIG) to serve as the electrode for producing Rime ice-type Bi-microstructures on the electrode. Stripping voltammetry was then used to detect Zn<sup>2+</sup> ions [149]. Other sensors for the detection of heavy metals using similar Bi-based stripping have been described in the literature [151,152].

The detection of chloride is useful for the determination of cystic fibrosis, in conjunction with conventional diagnostic

methods to enhance their overall efficacy [153]. Bujes-Garrido *et al.* [153] demonstrates the detection of halides. The sensor fabrication relies on the ED process, whereby Au is deposited on a polyethylene terephthalate (PET) substrate. The PET-Au electrodes can detect the halide ions using chronoamperometry. Their halide detection capability was verified from a sweat-carrying Gore-Tex sample. Another chloride sensor is demonstrated by Possanzini *et al.* [154], whereby ED was used to form Ag nanoparticles on single-thread fabrics. The resulting sensor enabled the detection of chloride ions within a range of 1 mM to 115 mM, measured as a function of current [154].

#### pH sensors

While the detection of specific analytes and metabolites confers significant healthcare value, the pH of the bodily fluid is also a useful measure for monitoring the patient's health. Specifically,

TABLE 5

Analyte	Electrodeposited Material	Detection Modality	Limit-of-Detection	Ref.
Temp	Pt nanoparticle decorated carbonized silk fibroin nanofiber (CSNF-Pt)	Resistivity across CSNF-Pt	35 °C	[139]
Strain	MnO <sub>x</sub> on PEDOT:PSS coated lycra	Relative capacitance change of the stretchable supercapacitor	40% strain	[140]
Glucose Humidity pH	PEDOT, Ag/AgCl, Au, Prussian blue, PANI	Glucose: Chronoamperometric detection of glucose oxidation Humidity: Impedance changes of the PEDOT film pH: Open-circuit potential changes between PANI and reference electrode	Not reported	[141]
Temp Proximity Pressure	Ni on polyacrylonitrile nanofibers	Temperature: Resistivity of nanofibers Proximity: Voltage change between bottom and top nanofiber layers Pressure: Resistivity between two nanofiber layers	Temp: 26.5 °C Proximity: 1 mm Pressure: 10 kPa	[142]
Pressure	MnO <sub>2</sub> on Ni skeletons supported by a carbon nanotube film	Changes in current of assembled microbattery	0.48 Pa	[143]
Lactate	Prussian blue on elastomeric Au fibers	Chronoamperometric detection of current through fibers	0.137 mM	[145]
Glucose	Cotton-like Au microspheres on carbon cloth	Chronoamperometric detection of glucose oxidation	0.78 μΜ	[146]
Na <sup>+</sup>	Na <sup>+</sup> & K <sup>+</sup> : PEDOT:PSS	Na <sup>+</sup> & K <sup>+</sup> : Potentiometric changes in PEDOT:PSS film	Na <sup>+</sup> : 10 mM	[147]
$K^+$			K <sup>+</sup> : 2 mM	
Cu <sup>2+</sup>	Cu <sup>2+</sup> : Cu onto working electrode	Cu <sup>2+</sup> : Peak currents of Cu redox during SWV	Cu <sup>2+</sup> : 100 μg/mL	
Glucose	Glucose: Prussian blue onto carbon working electrode	Glucose: Amperometric detection of glucose oxidation	Glucose: 75 μM	
			Caffeine: Not reported	
Caffeine	Caffeine: n/a	Caffeine: Peak currents of caffeine redox via DPV	C-2+ F M	[1.40]
Ca <sup>2+</sup> Cl <sup>-</sup>	rGO and Au nanoparticles on carbon working electrode	Voltages changes in the ion-to-electron transducer	Ca <sup>2+</sup> : 5 μM Cl <sup>-</sup> : 500 μM	[148]
Zn <sup>2+</sup>	Bi on laser-induced graphene (LIG)	Stripping current response from Zn <sup>2+</sup> during SWASV	40 ppb	[149]
Cd <sup>2+</sup> Pb <sup>2+</sup>	Bi on LIG/LIG fibers (LIGF)	Stripping current response of Cd <sup>2+</sup> and Pb <sup>2</sup> during SWASV	Cd <sup>2+</sup> & Pb <sup>2+</sup> : 0.4 μg/L	[151]
Cl <sup>-</sup> Br <sup>-</sup> I <sup>-</sup>	Ag nanoparticles on screen-printed carbon electrodes	Anodic peak currents of halides during LSV scans	CI <sup>-</sup> : $3 \times 10^{-6}$ M Br <sup>-</sup> : $5 \times 10^{-6}$ M I <sup>-</sup> : $5 \times 10^{-6}$ M	[153]
Cl <sup>-</sup> pH	Ag/AgCl nanoparticles (for Cl <sup>-</sup> ) or PEDOT: BTB (for pH) on PEDOT:PSS coated threads	Electrochemically gated current response	Cl <sup>-</sup> : 0.3 mM Linear range: pH 4.2–7	[154]
pН	IrO <sub>2</sub> on Argenmesh, Ristop silver, and stainless steel mesh	Open-circuit voltage of the various fabrics	Linear range: pH 4–8	[156]
рН	IrO <sub>2</sub> on PEDOT:PSS	Electrochemically gated voltage response	Linear range: pH 3-11	[157]

sweat samples that deviate from typical physiological pH (5.5) can be indicative of acidosis, electrolytic imbalance, cystic fibrosis, osteoporosis, and bone mineral loss [155]. In this sense, Zamora *et al.* [156] used  $IrO_x$  films prepared by ED to achieve pH measurement [156]. Scavetta *et al.* [157] demonstrated how this  $IrO_2$  could be utilized in the production of a bandage that can monitor the pH at the applied area in real-time. Therein, the functional textile is produced by performing the ED of  $IrO_x$  on PEDOT:PSS films, which are later integrated into the textile. The determination of pH is achieved by cyclic voltammetry, in which the peak shift toward negative potential denotes basic pH.

Conductive polymers prepared by EP are also useful for wearable sensor platforms, especially considering that organic materials are more biocompatible than inorganic materials derived by ED. Lee *et al.* [141] demonstrated the integration of PEDOT, Ag, Prussian blue, porous Au, and electrodeposited PANi to produce a wearable pH sensor (Fig. 11). Hydrogel-based microneedles, which dissolve in contact with sweat to release the cargo, are also integrated into the wearable device to facilitate transdermal drug delivery [141]. The determination of pH was achieved using two PANi-deposited electrodes. Moreover, the authors report this sensor's ability to detect glucose for a more comprehensive health monitoring.

In another study, Au-functionalized electrospun polymethyl methacrylate (PMMA) nanofibers collected on Cu frames were utilized as the substrate for the ED of Pd and PdO nanostructures, and the pH sensing capabilities of this composite was demonstrated [158]. To produce the PMMA fibers, a 10% solution of

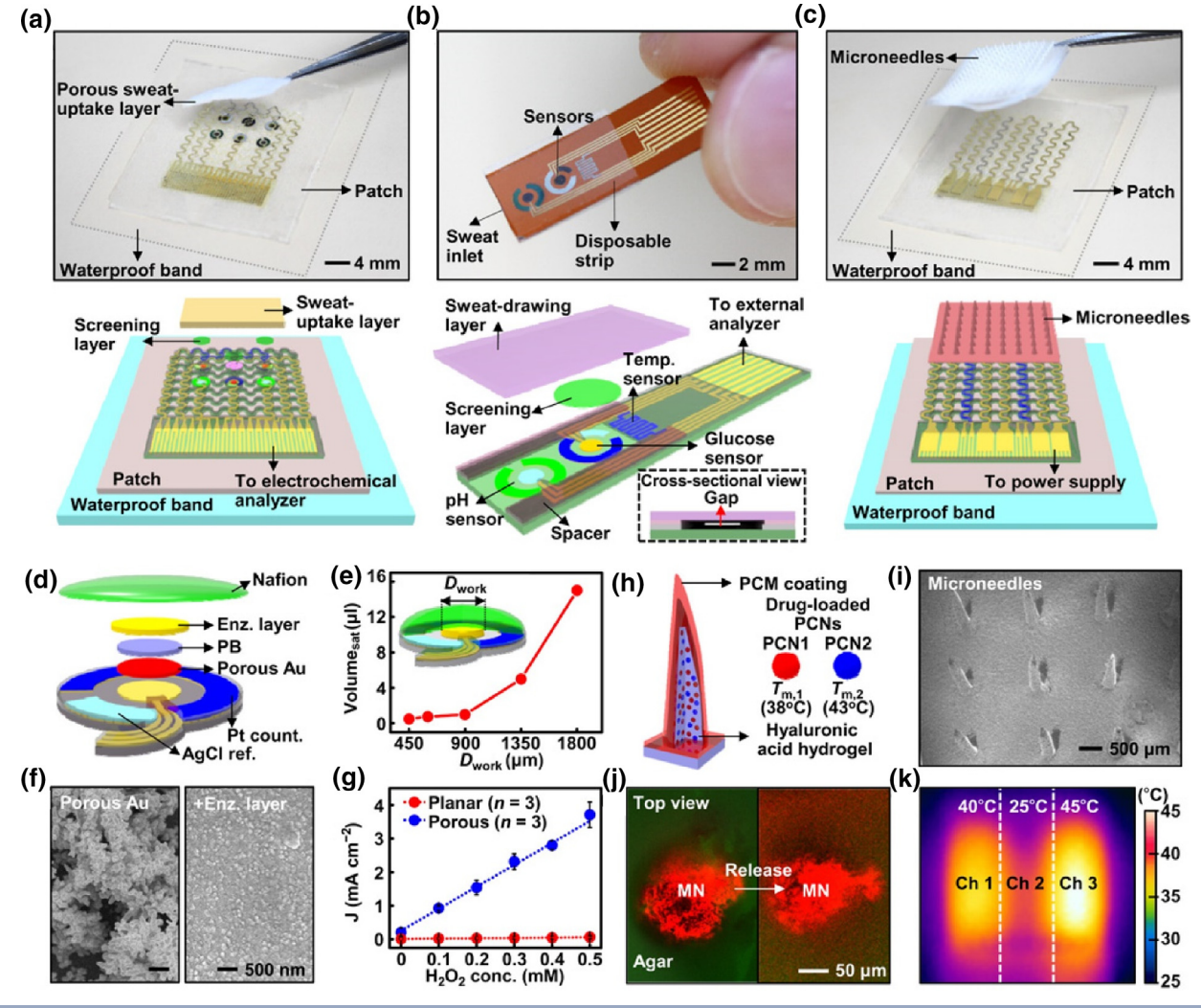


#### FIGURE 1

(a) Optical camera image (top; dotted line, edges of the patch) and schematic (bottom) of the wearable sweat monitoring patch. A porous sweat-uptake layer is placed on a Nafion layer and sensors. (b) Optical camera image (top) and schematic (bottom) of the disposable sweat monitoring strip. (c) Optical camera image (top; dotted line, edges of the patch) and schematic (bottom) of the transdermal drug delivery device. Replacement-type microneedles are assembled on a three-channel thermal actuator. (d) Schematic drawing of the glucose sensor in an exploded view. PB, Prussian blue. (e) Minimum volume of the artificial sweat required for sensing with different sizes of the glucose sensor. (f) Scanning electron microscope (SEM) images before (left) and after (right) immobilization of the enzyme (enz.) on the porous Au electrode. (g) Comparison of the H<sub>2</sub>O<sub>2</sub> sensitivity in the planar and porous Au electrode deposited with Prussian blue at different H<sub>2</sub>O<sub>2</sub> concentrations. (h) Schematic of the drug-loaded microneedles. The right inset describes details of different PCNs. (i) SEM image of the microneedles. (j) Confocal microscope images of the released dye from microneedles (MN) (top view) into the 4% agarose gel (green, agar; red, dye). (k) Infrared (IR) camera image of the three-channel (ch) thermal actuator. Reproduced with the permission of Ref. [141], copyright 2018, the American Association for the Advancement of Science (AAAS).

PMMA containing Au nanoparticles is electrospun at 15 kV and collected on Cu frames, creating a non-woven mesh with micron-sized fibers. The Au-PMMA fibers are further functionalized with Pd and PdO with an ED process, then annealed in air for 4 hours at 150 °C. The resulting PdO@Pd@Au@PMMA structure is used for the pH detection using EIS, whereby the total impedance correlates to pH of the solution. The authors report the ability to accurately determine the pH in solutions as small as 250 nL with a range of 4 to 8, well within the range of interest in typical physiologies [158].

## **ED-based Signal Transduction/Amplification**

In this review, ED has allowed for the preparation of materials, and composites of materials, that perform the function of recognizing and binding an analyte species of interest. But in a limited number of cases, the transduction process itself has involved ED as a means for amplifying the available sensor signal. The most prominent work in this category is that of Chad Mirkin and coworkers [25,35,159-161] who first described this concept in 2002 (Fig. 1) [25]. In the original experiments, signal amplification of a DNA hybridization and detection experiment was demonstrated when ss-DNA capture strands were immobilized between two lithographically patterned metal electrodes. The recognition and binding of complimentary ss-DNA-labeled Au nanoparticles produced a conductive pathway between the source and drain electrodes, and the conductance was increased by incubating the surface with an electroless Ag plating solution that selectively deposited Ag onto the Au nanoparticles, "reinforcing" the conductive pathway. Subsequent work with electroless amplification schemes has primarily exploited colorimetric and spectroscopic read-outs rather than electronic detection strategies [162].

Liming Dai and coworkers [163] described a related paradigm that involves two electroless particle deposition processes. First, Au nanoparticles are deposited on a porous nickel electrode. A α-fetoprotein antigen (AFP) antibody (Ab) is then assembled onto these Au nanoparticles and this capture surface is used for binding AFP from solution for a specified time. Finally, Ag nanoparticles, functionalized with a secondary Ab for AFM, is exposed to this surface to form a sandwich at each bound AFM molecule. Anodic stripping voltammetry (ASV) for Ag then provides a highly sensitive detection for the bound Ag and therefore, the bound AFP. A detection limit down of 2.3 pg/mL was thereby demonstrated [163]. Crooks and coworkers [164,165] have developed related, Ag-based electrochemical transduction schemes for immunosensors that also leverage the ultra-high sensitivity inherent to ASV.

A closely-related transduction and amplification strategy has recently been demonstrated for the detection of K<sup>+</sup> by Samori and coworkers [72]. In case, a 3-aminopropyl)triethoxysilane (APTES) adhesive layer was used to functionalize the glass surface between source and drain electrodes and bare Au nanoparticles were self-assembled onto the APTES functionalized glass in this gap. Then, a K<sup>+</sup> organic ionophore (DTDB-18C6 macrocycle) was adsorbed onto the Au nanoparticles. Repeating the Au nanoparticle + DTDB-18C6 self-assembly steps decreased the impedance of the device, and increased K + sensitivity. μM con-

centrations of K<sup>+</sup> were thereby detected, with good selectivity relative to other common cations [72].

#### **Conclusions**

The confluence of electrodeposition and electropolymerization with chemical sensing/biosensing is relatively recent, having occurred just forty years ago (1980–2020). The first 20 years of this period were dominated by the realization of applications that exploited conductive polymers as transducers. During the period from 2000–2010, an expanding ability to electrochemically synthesize low-dimensional materials, especially metal, oxide, and semiconductor nanoparticles and nanowires, powered innovations in chemical and biological sensor architectures that increasingly exploited ED and EP synthesized components. Advances in gas sensing were particularly prominent during this period. It was also discovered that highly dispersed metal microelectrodes, prepared by ED, could serve as versatile, easily programmed, transducers in biosensors.

The last five years, reviewed here, impactful new trends and innovations have emerged. These include:

- ED-based **transduction/amplification schemes** involving the target-catalyzed electro-reduction of a silver or copper deposit that can be selectively electro-oxidized to generate electrical signal. These ED-based schemes are analogous to ELISAs (enzyme-linked immunosorbent assays) in the sense that signal from very low concentrations of target can be integrated to enhance sensitivity.
- Precise ED control of the morphology of microscopic gas sensor transducers – mainly aimed at increasing the curve area:volume ratio of these structures – has enabled improvements to response speed and sensitivity.
- ED-fabrication of nanoscopic and lowdimensional transducers including nanoparticles, nanowires, and layers of 2D materials – aided by the precise electrochemical control of these processes.
- The development of **molecular filtering layers** that can be deposited electrolessly and are capable of super-charging the performance of H<sub>2</sub> gas sensors. Applications of this technology to size-selective biosensing of proteins, for example, can readily be imagined in the future.
- The single-step EP of electronically conductive polymer composites with engineered virus particles for use as bioaffinity layers in biosensors.
- Penetration of ED/EP methods, in many creative ways, into the rapidly growing subfield of wearable sensors. The development of multiplexed sweat sensors for metabolites, including glucose, represents a new and exciting application for ED-enabled sensor technologies.

More generally, methods for applying ED/EP to the preparation of capture or affinity layers for chemical sensors and biosensors are in their infancy. This application has many challenges relating to molecular level control of the presentation of these receptors, optimization of electrical conductivity, permeability, and porosity, and receptor coverage representing a host of future challenges for the field.

#### Data availability

No data was used for the research described in the article.

## **Declaration of Competing Interest**

The authors declare that they have no known competing financial interests or personal relationships that could have appeared to influence the work reported in this paper.

## **Acknowledgements**

This work was supported by the US National Science Foundation (NSF) through grants CBET 2149631 and CHE 2201042. Additional support was provided by the National Research Foundation of Korea (NRF) grant (NRF2019M3D1A2104100) and the Nano-Convergence Foundation (no. 20000230) funded by the Korean Government.

#### References

- [1] A.F. Diaz, J.A. Logan, J Electroanal Chem Interfacial Electrochem 111 (1980) 111-114.
- [2] A.F. Diaz et al., J Electroanal Chem 129 (1981) 115-132.
- [3] R.J. Waltman, J. Bargon, A.F. Diaz, J Phys Chem 87 (1983) 1459-1463.
- [4] A.F. Diaz, B. Hall, IBM J Res Dev 27 (1983) 342-347.
- [5] A.F. Diaz, K.K. Kanazawa, G.P. Gardini, J Chem Soc Chem Commun (1979) 635-636.
- [6] M. Sato, S. Tanaka, K. Kaeriyama, Synth Met 14 (1986) 279-288.
- [7] G. Heywang, F. Jonas, Adv Mater 4 (1992) 116-118.
- [8] J. Janata, Analyst 119 (1994) 2275-2278.
- [9] J. Janata, M. Josowicz, Nat Mater 2 (2003) 19-24.
- [10] J. Janata, Chem Rev 90 (1990) 691-703.
- [11] M. Josowicz, J. Janata, Anal Chem 58 (1986) 514–517.
- [12] J.J. Miasik, A. Hooper, B.C. Tofield, J Chem Soc 82 (1986) 1117.
- [13] M. Umana, J. Waller, Anal Chem 58 (1986) 2979-2983.
- [14] I. Taniguchi et al., Anal Sci 2 (1986) 587-588.
- [15] N.C. Foulds, C.R. Lowe, J Chem Soc, Faraday Trans 1 82 (1986) 1259-1264.
- [16] E.C. Walter et al., J Phys Chem B 106 (2002) 11407-11411.
- [17] M.P. Zach, K.H. Ng, R.M. Penner, Science 290 (2000) (1979) 2120-2123.
- [18] F. Favier et al., Science 293 (2001) (1979) 2227-2231.
- [19] E.C. Walter, F. Favier, R.M. Penner, Anal Chem 74 (2002).
- [20] H.X. He, C.Z. Li, N.J. Tao, Appl Phys Lett (2001).
- [21] K. Ramanathan et al., Nano Lett 4 (2004) 1237-1239.
- [22] M. Yun et al., Nano Lett 4 (2004) 419-422.
- [23] Y. Im et al., Small 2 (2006) 356-358.
- [24] S. Babu et al., Microfluid Nanofluidics 1 (2005) 284-288.
- [25] S.-J. Park, T.A. Taton, C.A. Mirkin, Science 295 (2002) (1979) 1503–1506.
- [26] G.W. Hacker, Elsevier (1989) 297-321.
- [27] X. Su, S.J. O'Shea, S.F.Y. Li, Chem Commun (2001) 755-756.
- [28] E.J. Menke et al., Nat Mater 5 (2006) 914–919.
- [29] C. Xiang, Y. Yang, R.M. Penner, Chem Commun (2009) 859-873.
- [30] F. Yang, D.K. Taggart, R.M. Penner, Nano Lett 9 (2009) 2177–2182.
- [31] L. Soleymani et al., Appl Phys Lett 95 (2009) 143701.
- [32] L. Soleymani et al., Angew Chem Int Ed 48 (2009) 8457-8460.
- [33] L. Soleymani et al., Nat Nanotechnol 4 (2009) 844-848.
- [34] A.T. Sage et al., Acc Chem Res 47 (2014) 2417-2425.
- [35] S.O. Kelley et al., Nat Nanotechnol 9 (2014) 969-980.
- [36] J.H. Tang et al., Sci Rep 6 (2016) 1-9.
- [37] W. Wang, H. Guo, R.A. Jones, Dalton Trans 48 (2019) 14440–14449.
- [38] A. Ionescu et al., ACS Appl Mater Interfaces 7 (2015) 4019-4028.
- [39] M. Abe et al., Inorg Chem 54 (2015) 11061-11063.
- [40] S. Napierała et al., Electrochim Acta 369 (2021).
- [41] A. Kassa, A. Abebe, M. Amare, Electrochim Acta 384 (2021) 138402.
- [42] A. Friedman et al., ACS Catal 8 (2018) 5024-5031.
- [43] A. GhavamiNejad et al., Colloids Interface Sci Commun 6 (2015) 5-8.
- [44] Z. Cai et al., ACS Sustain Chem Eng 5 (2017) 571-579.
- [45] M. Gao et al., Electrochim Acta 228 (2017) 522-527.
- [46] W. da Silva, A.C. Queiroz, C.M.A. Brett, Electrochim Acta 347 (2020) 136284.
- [47] J. Cai et al., Small 13 (2017) 1–12.
- [48] A. Bhasin et al., Anal Chem 92 (2020) 6654-6666.
- [49] J.M. Moon, Y. Hui Kim, Y. Cho, Biosens Bioelectron 57 (2014) 157–161.
- [50] O. Ouerghi et al., J Electroanal Chem 501 (2001) 62-69.

- [51] T. Yang et al., Colloids Surf B Biointerfaces 83 (2011) 179-182.
- [52] W. Chen et al., Electrochem Solid St 11 (2008).
- [53] Y. Shao, Y. Jin, S. Dong, Electrochem Commun 4 (2002) 773-779.
- [54] H. Sakaguchi et al., Science 310 (2005) (1979) 1002-1006.
- [55] V. Subramanian, D.C. Martin, Nano Lett 21 (2021) 9077-9084.
- [56] G. Herlem, F. Picaud, J Phys Chem A 125 (2021) 1860-1869.
- [57] S.E. Fosdick et al., Angew Chem Int Ed 52 (2013) 10438–10456.
- [58] F. Goodridge, C.J.H. King, A.R. Wright, Electrochem Acta 22 (1977) 1087-
- [59] J.R. Backhurst et al., J Electrochem Soc 116 (1969) 1600-1607.
- [60] J. Ji et al., J Mater Chem C Mater 8 (2020) 11499-11507.
- [61] G. Salinas et al., ChemElectroChem 9 (2022) 1-9.
- [62] Z. Chen, E. Villani, S. Inagi, Curr Opin Electrochem 28 (2021) 100702.
- [63] N. Shida, Y. Zhou, S. Inagi, Acc Chem Res 52 (2019) 2598–2608.
- [64] L. Bouffier et al., Annu Rev Anal Chem 14 (2021) 65-86.
- [65] C. Fradin et al., J Colloid Interface Sci 590 (2021) 260-267.
- [66] D. Wang et al., Electrochim Acta 401 (2022).
- [67] Y. Koizumi et al., Nat Commun 7 (2016) 1-6.
- [68] T. Watanabe et al., ACS Macro Lett 7 (2018) 551-555.
- [69] N. Shida et al., Synth Met 266 (2020) 116439.
- [70] K. Janzakova et al., Nat Commun 12 (2021) 1-11.
- [71] A. Kumar et al., Sci Rep 12 (2022) 1–11.
- [72] V. Montes-García et al., Adv Funct Mater 31 (2021) 2008554.
- [73] J. Hu et al., Sens Actuators B Chem 346 (2021) 130474.
- [74] P. Bazylewski et al., ACS Omega 5 (2020) 643-649.
- [75] Y. Zhang et al., J Am Chem Soc 141 (2019) 14643-14649.
- [76] P.R.R. Chansi et al., Nanoscale 12 (2020) 21719-21733.
- [77] R. Jin et al., Sens Actuators B Chem 327 (2021) 128922.
- [78] M.L. Xu et al., J Agric Food Chem 65 (2017) 6719-6726.
- [79] M. Liu et al., Biosens Bioelectron 130 (2019) 174-184.
- [80] M.J. Kangas et al., Crit Rev Anal Chem 47 (2017) 138-153. [81] Y.Y. Broza et al., Chem Rev 119 (2019) (1817) 11761-11771.
- [82] C.F. Markwalter et al., Chem Rev 119 (2019) 1456-1518.
- [83] M. Labib, E.H. Sargent, S.O. Kelley, Chem Rev 116 (2016) 9001–9090.
- [84] S. Wustoni et al., Adv Mater Technol 5 (2020) 1-9.
- [85] J. Park et al., ACS Sens 5 (2020) 1363-1373.
- [86] A. Bhasin et al., Nano Lett 18 (2018) 3623-3629.
- [87] A. Bhasin et al., Anal Chem 93 (2021) 11259-11267.
- [88] R.D. Crapnell et al., Sensors (Switzerland) 19 (2019).
- [89] L. Moreira Gonçalves, C. Opin, Electrochem 25 (2021) 100640.
- [90] L. Zhang et al., Biosens Bioelectron 100 (2018) 235-241.
- [91] J. Yang, Y. Hu, Y. Li, Biosens Bioelectron 135 (2019) 224-230.
- [92] M. Wei et al., J Electroanal Chem 842 (2019) 184-192.
- [93] M. Dehghani, N. Nasirizadeh, M.E. Yazdanshenas, Mater Sci Eng C 96 (2019)
- [94] W. Hai et al., Sens Actuators B Chem 260 (2018) 635-641.
- [95] J. Wang et al., Anal Chem 91 (2019) 13831-13837.
- [96] X. Bin, E.H. Sargent, S.O. Kelley, Anal Chem 82 (2010) 5928-5931.
- [97] S. Su et al., Small 12 (2016) 3794–3801.
- [98] S. Mahshid et al., J Phys Chem C 120 (2016) 21123-21132.
- [99] P. Sadat Mousavi et al., Nat Chem 12 (2020) 48-55.
- [100] J. Peng et al., Microchim Acta 185 (2018) 1-8.
- [101] A. Ganguly, J. Benson, P. Papakonstantinou, ACS Appl Bio Mater 1 (2018) 1184-1194.
- [102] J.T. Cao et al., Biosens Bioelectron 99 (2018) 92-98.
- [103] G. Xu et al., Sens Actuators B Chem 287 (2019) 428-436.
- [104] C. Chen et al., RSC Adv 11 (2021) 37917-37922.
- [105] M. Shariati et al., Anal Chim Acta 1048 (2019) 31-41.
- [106] D.H. Shin et al., Sens Actuators B Chem 264 (2018) 216–223.
- [107] R. Xi et al., Sensors (Switzerland) 19 (2019).
- [108] A.R. Rajamani et al., J Phys Chem C 120 (2016) 22398–22406.
- [109] M. Zea et al., ACS Appl Mater Interfaces 11 (2019) 15160-15169.
- [110] S. Traipop et al., Sci Rep 11 (2021).
- [111] K.K. Naik et al., ACS Appl Mater Interfaces 9 (2017) 23894-23903.
- [112] T. Gupte et al., ACS Appl Mater Interfaces 11 (2019) 28154-28163.
- [113] X. Qin et al., Anal Chem 90 (2018) 11622-11628.
- [114] D. Tang et al., ACS Appl Mater Interfaces 13 (2021) 46225-46232. [115] M. Sharifuzzaman et al., Small 16 (2020).
- [116] P. Lin, F. Yan, H.L.W. Chan, ACS Appl Mater Interfaces 2 (2010) 1637–1641. [117] A. Dey, Mater Sci Eng B 229 (2018).
- [118] W.-T. Koo et al., ACS Nano 14 (2020) 14284-14322.
- [119] N. Ramgir et al., Colloids Surfaces A Physicochem. Eng. Asp. 439 (2013) 101-

- [120] X. Chen et al., Sensors Actuators B Chem. 177 (2013) 178–195.
- [121] E. Llobet, Sens Actuators B Chem 179 (2013) 32-45.
- [122] A. Collins et al., Science 287 (2000) 1801–1804.
- [123] V. Schroeder et al., Chem Rev 119 (2019) 599-663.
- [124] T. Han et al., Sens Actuators A Phys 291 (2019) 107-143.
- [125] M.N. Norizan et al., RSC Adv 10 (2020) 43704-43732.
- [126] X. Li et al., ACS Sens 2 (2017) 282-289.
- [127] H. Liu, R.M. Penner, J Phys Chem B 104 (2000) 9131-9139.
- [128] Gribkova OL, Kabanova VA, Nekrasov AA, n.d.
- [129] M. Mateos et al., ACS Sens 4 (2019) 740-747.
- [130] P. Ranka, V. Sethi, A.Q. Contractor, Sens Actuators B Chem 261 (2018) 11-21.
- [131] H.-J. Cho et al., ACS Sens 3 (2018) 2152-2158.
- [132] C. Wang et al., Sens Actuators B Chem 292 (2019) 270-276.
- [133] Z. Pan et al., J Mater Chem A Mater 7 (2019) 1287-1299.
- [134] Y. Zhang et al., J Mater Sci Mater Electron 27 (2016) 1817-1827.
- [135] J. Shi et al., Sensors Actuators B Chem 230 (2016) 736-745.
- [136] J.-S. Jang et al., ACS Appl Mater Interfaces 9 (2017).
- [137] W.T. Koo et al., ACS Nano 11 (2017) 9276-9285.
- [138] R.M. Penner, Acc Chem Res 50 (2017) 1902-1910.
- [139] Z. Yang et al., ACS Appl Mater Interfaces 14 (2022) 18110-18119.
- [140] A. Pullanchiyodan et al., ACS Appl Mater Interfaces 13 (2021) 47581-47592.
- [141] H. Lee et al., Sci Adv 3 (2017).
- [142] H. Seok Jo et al., Sci Rep 10 (2020) 1-12.
- [143] B. He et al., J Mater Chem A Mater 6 (2018) 14594-14601.
- [144] F. Alam et al., Biosens Bioelectron 117 (2018) 818-829.
- [145] R. Wang et al., Talanta 222 (2021) 121484.
- [146] Q. Peng et al., Anal Chim Acta 1159 (2021) 338442.
- [147] M. Bariya et al., ACS Nano 12 (2018) 6978-6987.
- [148] G. Xu et al., Sens Actuators B Chem 297 (2019) 126743.
- [149] X. Xuan et al., Microchim Acta 188 (2021) 1-11.
- [150] I. Švancara et al., Electroanalysis 22 (2010) 1405-1420.
- [151] S.E. Jeong et al., Microchem J 172 (2022) 106950.
- [152] G. Zhao et al., Sens Actuators B Chem 350 (2022).

- [153] J. Bujes-Garrido et al., Anal Chim Acta 1012 (2018) 42-48.
- [154] L. Possanzini et al., Sci Rep 10 (2020) 1-14.
- [155] L. Manjakkal, S. Dervin, R. Dahiya, RSC Adv 10 (2020) 8594-8617.
- [156] M.L. Zamora et al., Sens Actuators B Chem 260 (2018) 601-608.
- [157] F. Mariani et al., ACS Sens 6 (2021) 2366-2377.
- [158] V.C. Diculescu et al., Sci Rep 9 (2019) 1-12.
- [159] I.N. Larkin et al., Anal Chem 92 (2020) 7845-7851.
- [160] Z. Wang et al., Nanoscale 6 (2014) 3110-3115.
- [161] K. Nam et al., J Mater Chem 22 (2012) 23348-23356.
- [162] A.W. Scott et al., Bioconjug Chem 28 (2017) 203-211.
- [163] C. Zhao et al., Sci Bull (Beijing) 64 (2019) 1272-1279.
- [164] Y. Peng et al., ACS Sens 6 (2021) 1111-1119.
- [165] N.E. Pollok et al., ACS Appl Nano Mater 4 (2021) 10764-10770.
- [166] S. Chen et al., ACS Appl Mater Interfaces 9 (2017) 5430-5436.
- [167] Y. Li et al., Carbohydr Polym 195 (2018) 505-514.
- [168] N. Karimian et al., ACS Sens 3 (2018) 1291-1298.
- [169] J. Fu et al., Sens Actuators B Chem 287 (2019) 503-509.
- [170] A.B. Hashkavayi, J.B. Raoof, Biosens Bioelectron 91 (2017) 650-657.
- [171] S.R. Torati et al., Sens Actuators B Chem 243 (2017) 64-71.
- [172] Z. Lu et al., Microchim Acta 184 (2017) 4731-4740.
- [173] A. Dey, Mater Sci Eng B 229 (2018) 206-217.
- [174] O. DTSEM Salt Lake Technical Center, n.d.
- [175] C. Wang et al., J Alloys Compd 790 (2019) 363-369.
- [176] OSHA, 2021.
- [177] H. Steinebach et al., Sens Actuators B Chem 151 (2010) 162-168.
- [178] The National Institute for Occupational Safety and Health (NIOSH), 2011.
- [179] L. Antonio Panes-Ruiz et al., n.d.
- [180] D. Yan et al., J Alloys Compd 735 (2018) 718–727.
- [181] D.v. del Orbe et al., Sens Actuators B Chem 329 (2021) 129129.
- [182] Y. Zhao et al., Sens Actuators A Phys 320 (2021) 112574.
- [183] W. Na et al., Interfaces 7 (2020) 1902006.
- [184] O. Alev et al., J Alloys Compd 826 (2020) 154177.